Article:
Temple, IP, Logantha, SJRJ, Absi, M et al. (20 more authors) (2016) Atrioventricular Node Dysfunction and Ion Channel Transcriptome in Pulmonary Hypertension. Circulation: Arrhythmia and Electrophysiology, 9 (12). e003432. ISSN 1941-3149

https://doi.org/10.1161/CIRCEP.115.003432

Atrioventricular node dysfunction and ion channel transcriptome in pulmonary hypertension

Short title: AV node dysfunction in pulmonary hypertension

Ian P. Temple, BSc, MBChB, MRCP, PhD, [1*]; Sunil Jit R.J. Logantha, BPharm, MSc, PhD[1*]; Mais Absi, PhD[1]; Yu Zhang, BSc[1]; Eleftheria Pervolaraki, BSc, MSc, PhD[2]; Joseph Yanni, MB ChB, MSc, PhD[1]; Andrew Atkinson, MBioMedSci, MPhil[1]; Maria Petkova, BSc, MRes[1]; Gillian M. Quigley, BSc, PhD[1]; Simon Castro, MPhys, PhD[3]; Mark Drinkhill, BSc, PhD[2]; Heiko Schneider, MRCP, PhD[1]; Oliver Monfredi, BSc, MBChB PhD[1]; Elizabeth Cartwright, BSc, MSc, PhD[1]; Min Zi, MD, MPhil[1]; Tomoko T. Yamanushi, BSc, MS, PhD[4]; Vaikom S. Mahadevan, MBBS, MD, FRCP, FACC[5]; Alison M. Gurney, BSc, PhD, FRSB, FBPhS[1]; Ed White, BSc, PhD[2]; Henggui Zhang, BSc, MSc, PhD[3]; George Hart, MA, DM, FRCP, FACC[1]; Mark R. Boyett, BSc, PhD, FSB, FRCP[1†]; Halina Dobrzynski, BSc, PhD[1†];

*Joint first authors; [†]joint senior authors

[1] Cardiovascular Sciences, University of Manchester, Manchester, UK; [2]School of Biomedical Sciences, University of Leeds, Leeds, UK; [3]School of Physics and Astronomy, University of Manchester, Manchester, UK; [4]Kagawa Prefectural College of Health Sciences, Takamatsu, Japan; [5]Department of Medicine, University of California, San Francisco, USA

Corresponding author: Professor Mark Boyett; Cardiovascular Sciences, University of Manchester, Core Technology Facility, 46 Grafton Street, Manchester M13 9NT, UK;

Tel: +44 161 275 1192 Fax: +44 161 275 1183 Email: mark.boyett@manchester.ac.uk

Journal Subject Terms: Arrhythmias, Animal Models of Human Disease, Ion Channels/Membrane Transport, Gene Expression and Regulation, Heart Failure, Pulmonary Hypertension

Word count: 8,385

Abstract

Background – Heart block is associated with pulmonary hypertension and the aim of the study was to test the hypothesis that the heart block is the result of a change in the ion channel transcriptome of the atrioventricular node.

Methods and Results – The most commonly used animal model of pulmonary hypertension, the monocrotaline-injected rat, was used. The functional consequences of monocrotaline injection were determined by echocardiography, ECG recording and electrophysiological experiments on the Langendorff-perfused heart and isolated atrioventricular node. The ion channel transcriptome was measured by quantitative PCR, and biophysically-detailed computer modelling was used to explore the changes observed. Following monocrotaline injection: echocardiography revealed the pattern of pulmonary artery blood flow characteristic of pulmonary hypertension as well as right-sided hypertrophy and failure; the Langendorff-perfused heart and isolated atrioventricular node revealed dysfunction of the atrioventricular node (e.g. 50% incidence of heart block in isolated AV node); and quantitative PCR revealed a widespread downregulation of ion channel and related genes in the atrioventricular node (e.g. >50% downregulation of $Ca_v1.2/3$ and HCN1/2/4 channels). Computer modelling predicted that the changes in the transcriptome if translated into protein and function would result in heart block.

Conclusions – Pulmonary hypertension results in a derangement of the ion channel transcriptome in the atrioventricular node and this is the likely cause of atrioventricular node dysfunction in this disease.

Key words: Pulmonary hypertension, Arrhythmias, Atrioventricular node, Heart block, Ion channels

Introduction

Pulmonary arterial hypertension (PHT) is a disease characterised by raised pulmonary vascular resistance. It has a poor prognosis typically resulting in progressive right ventricular failure and death. The incidence of arrhythmias in patients with PHT is high.[1-3] All forms of supraventricular tachycardia are more common in PHT with studies suggesting an incidence of ~3%/year and a prevalence of supraventricular arrhythmia of ~12%.[3] Atrial flutter, atrial fibrillation and atrioventricular (AV) nodal reentrant tachycardia are common.[3,4] There is evidence of AV node dysfunction in PHT with a 14% incidence of first degree heart block, a mean PR interval of 180±50 ms (mean±SD) and 2% of patients requiring a pacemaker for high degree heart block on initial

screening of PHT patients.[1] This can be compared with an incidence of first degree heart block of 2.1% and mean PR interval of 160±22 ms (mean±SD) for men and 153±22 ms (mean±SD) for women in the general population.[5] Sleep apnoea causes PHT[6] and is associated with heart block (heart block during sleep has been described in up to 10% of patients with obstructive sleep apnoea).[7] Despite the evidence of a high burden of arrhythmias in patients with PHT, including dysfunction of the AV node, there is limited experimental data looking at the mechanisms of arrhythmia generation and the available data only concern arrhythmogenic mechanisms in the ventricle.[e.g.8] There are several animal models of PHT, but the monocrotaline model is the best characterised and most widely used.[e.g.9] Two studies using *in vivo* monitoring have demonstrated severe AV node dysfunction with heart block causing death in ~38% of monocrotaline-injected rats with PHT.[10,11] In the present study, the monocrotaline-injected rat was chosen to study the mechanisms underlying AV node dysfunction in PHT (see Supplementary Material for further validation of the monocrotaline-injected rat model). We show that the dysfunction is associated with widespread remodelling of the ion channel transcriptome.

Methods

200 g male Wistar rats received an intraperitoneal injection of monocrotaline (60 mg/kg) or volume-matched 0.9% saline (3 ml/kg). Rats were weighed and their clinical condition assessed twice weekly in the first 18 days and daily thereafter. Rats were assessed using echocardiography and ECG recording on day 0 immediately prior to injection, day 21 and immediately prior to termination. M-mode recordings were taken in the parasternal short axis view allowing recording of left ventricle anterior and posterior wall thickness and the internal diameter of the left ventricle in both systole and diastole. Right ventricle wall thickness was measured from M-mode recordings in the parasternal long axis view. Continuous wave Doppler recordings through the pulmonary artery were used to assess the pulmonary velocity profile. Monocrotaline-injected rats were sacrificed by stunning and cervical dislocation on day 28 or earlier if there was evidence of clinical deterioration (reduced movement, increased respiratory rate, piloerection, weight loss of >10 g over two days). A

saline-injected rat was sacrificed within 24 h of sacrifice of a monocrotaline-injected rat. Heart and lungs were excised and weighed. Telemetric recordings of ECGs from conscious and unrestrained male Wistar rats were made as previously described by Benoist *et al*.[12] The functioning of the AV node was measured in the Langendorff-perfused heart: the heart was mounted on a Langendorff column and retrogradely perfused with oxygenated Tyrode's solution at a temperature of 36.5˚C. Extracellular electrodes were used to record a 'pseudo-ECG'. RR, PR and QT intervals and QRS duration were measured. Pacing protocols were performed to measure atrial and ventricular effective refractory periods, AV node refractory periods and Wenckebach cycle length. Functioning of the AV node was also measured in the isolated AV node: a preparation was placed in a perfusion bath with oxygenated Tyrode's solution at 36.5˚C. Extracellular electrodes were used to record signals in the atrium and at the His bundle. Pacing protocols were performed to measure AV node refractory periods and Wenckebach cycle length. From the isolated AV node, intracellular actions potentials were also recorded with sharp microelectrodes.

Tissue was microdissected from different regions of the AV node: the AV node was sectioned at 50 μm in a cryostat. Sections 300 μm apart were stained with Masson's trichrome and immunolabelled for HCN4 and Cx43 to identify AV node tissues. Guided by this, AV node tissues were dissected with a sharp needle from remaining sections (haematoxylin and eosin stained). Total RNA was extracted using the MirVana kit, residual genomic DNA removed using TurboDNAse, RNA in each sample measured using the Qubit system, RNA reverse transcribed to produce cDNA using SuperScript VILO Mastermix with random hexamers, cDNA preamplified, and expression of different cDNAs corresponding to different mRNAs quantified using the TaqMan low density array card system (Life Technologies, USA). Expression was normalised to the abundance of a pair of housekeeper genes, B2M and PKG1, selected from 16 potential housekeeper genes as the most stable. The limma statistical package as implemented by RealTime Statminer software (Integromics) was used to compare mRNA expression in the control and monocrotaline-injected rats as well as compare mRNA expression in the different parts of the AV node. Multiple

comparisons in large bodies of data, such as in microarray data analysis, pose statistical challenges.[13,14] Typically, a correction is made when making multiple tests to avoid false-positive results (type I error),[13,14] but reducing the type I error increases the chance of false-negative results (type II error).[13,14] In relation to large data sets, Rothman[14] has argued that a policy of not making corrections for multiple tests is preferable. For comparison of mRNA expression in the control and monocrotaline-injected rats, the uncorrected *P* value is given in Table S3. Even without the argument from Rothman,[14] this can be justified, because each comparison is independent of the others (the conclusions of the present study do not depend on a group of differences being significant). Nevertheless, false discovery rate (FDR)-corrected *P* values are also given in Table S3 - multiple test corrections of the classical type are not commonly used in the analysis of microarray data and instead the FDR has become a standard for multiple tests correction.[13] In reporting both uncorrected and FDR-corrected *P* values from the limma test, we follow the example of earlier studies.[15,16] In Figs. 4-7, however, for simplicity the asterisks relate only to the FDR-corrected *P* value; cases in which the FDR-corrected *P* value is less than 0.2 (i.e. 20%) are highlighted with asterisks. An FDR of 20% (as we have used previously[16]) is permissive and means that ~20% of the 77 changes highlighted by asterisks, i.e. ~15, are false-positives. However, precise uncorrected and FDR-corrected *P* values are reported in Table S3 and the reader can make their own choice of what is acceptable. Rothman[14] states that "scientists should not be so reluctant to explore leads that may turn out to be wrong that they penalize themselves by missing possibly important findings". For comparison of mRNA expression in the different parts of the AV node, we report only FDR-corrected *P* values of <0.2 (using lower case letters) and <0.05 (using upper case letters) in Figs. 4-7, corresponding to false discovery rates of 20% and 5%. In this case, expression in various tissues is being compared and a multiple test correction is appropriate and we do not report uncorrected *P* values.

The potential consequences of the changes in transcripts were explored using a biophysically-detailed one-dimensional model (52.5 mm in length) consisting of segments of atrium

(15 mm), AV node (12.5 mm), Purkinje fibre (20 mm) and ventricle (10 mm), each represented by a well-established model of the corresponding action potential. To simulate the functional effects of PHT, the conductance of each ionic current was scaled based on the change in the corresponding mRNA. The 1D cable equation was solved using the Forward-Time Central-Space scheme with a space step of 0.1 mm and time step of 0.005 ms. Finally, expression of protein was investigated using immunohistochemistry. See Supplementary Material for expanded methods.

Results

PHT and right-sided heart failure

There was no significant difference in the body weight of control (saline-injected) and monocrotaline-injected rats on the day of injection (Table 1). During the following three weeks, the monocrotaline-injected rats gained significantly less weight such that they weighed 12% less than the control rats by the day of termination (Table 1). Despite the lower body weight, the monocrotaline-injected rats also had a 23% increase in heart weight and an 88% increase in lung weight compared to the control group (Table 1). The heart:body weight and lung:body weight ratios were significantly greater in the monocrotaline-injected rats on the day of termination suggestive of congestive heart failure (Table 1). Previous studies of the monocrotaline model using echocardiography have demonstrated a characteristic change in the pulmonary artery velocity profile from the typical rounded shape to a 'spike and dome' morphology with a reduced pulmonary artery acceleration time (PAAT) and an increased pulmonary artery deceleration (PAD) as pulmonary artery pressure increases.[17,18] In the present study, PAAT and PAD were used as surrogate measures of pulmonary artery pressure. On the day of termination, echocardiography demonstrated a reduced PVAT and increased PAD in the monocrotaline-injected rats (Fig. 1B; Table 1). This is evidence of PHT and monocrotaline-injected rats will now be referred to as PHT rats. There was evidence of right-sided heart failure in the PHT rats: there was right ventricular dilatation (increased right ventricular internal dimension) and hypertrophy (increased right ventricular diastolic wall thickness) and a 36% reduction in right ventricular fractional shortening (Fig. 1A; Table 1). In contrast, in the left ventricle there was no evidence of hypertrophy and there

was a *reduced* left ventricular internal diameter in the PHT rats - this was presumably the result of the raised right ventricular pressure pushing the ventricular septum into the left ventricle (Fig. 1A; Table 1). On the day of termination, the ECG measured *in vivo* in the anaesthetised rat showed a 98% increase in the QT interval, a 90% increase in the corrected QT interval (QTc interval) and a 9% increase in the RR interval (equivalent to 9% decrease in heart rate) in the PHT rats (Table 1); these changes are typical of heart failure.[19] Although no changes were seen in the PR interval (Table 1), the PR interval is determined by the position of the leading pacemaker site in the right atrium as well as the conduction velocity of the AV node. We have previously reported similar changes in the ECG measured *in vivo* in the conscious rat using telemetry.[12] In the UK, the Animal (Scientific Procedures) Act 1986 requires that monocrotaline-injected rats are sacrificed before they reach end-stage heart failure. However, one conscious freely-moving rat implanted with a telemetry system died naturally 28 days after injection with monocrotaline and the ECG recording showed that it died of heart block (Fig. 1C). This is consistent with earlier reports.[10,11]

Evidence from *in vitro* experiments of AV node dysfunction

It is possible that the AV node is supported *in vivo* by neurohumoral influences and, therefore, experiments were conducted on isolated heart preparations. First, experiments were conducted on the isolated Langendorff-perfused heart from 10 control and 11 PHT rats. Consistent with the *in vivo* measurements, there was a 141% increase in the QT interval, a 138% increase in QTc interval and a 144% increase in the ventricular effective refractory period in the PHT rats (Table 2). There was also a 24% increase in the atrial effective refractory period, but this was not significant (Table 2). Once again there was no change in the PR interval, but there was evidence of AV node dysfunction in the PHT rats: Fig. 2A shows typical AV node conduction curves from control and PHT rats – there was a significant increase in both the AV node effective and functional refractory periods (AVERP and AVFRP, respectively). The Wenckebach cycle length was increased (but not significantly) in the PHT rats. Although this increase was not significant, linear regression showed the Wenckebach cycle length to be significantly correlated with both the AVERP and AVFRP and

this suggests that PHT does tend to prolong the Wenckebach cycle length (Fig. 2B). Experiments were also conducted on an isolated right atrial preparation containing the AV node from 10 control and 11 PHT rats. Electrograms were recorded from above the His bundle and examples are shown in Fig. 2C – both atrial and His bundle electrograms were recorded at the recording site. There was normal AV node conduction in the control rat, but complete heart block in the PHT rat with dissociation of the atrial and His bundle electrograms (Fig. 2C). There was a 50% incidence of complete heart block in the PHT rats (6 of 12 PHT rats) compared to 0% in the control group (0 of 10 control rats); the difference is statistically significant (Fisher's exact test; P=0.015; Table 2). In the remaining 6 PHT rat preparations in which AV node conduction persisted, there were increases in the AH interval (interval between atrial and His bundle electrograms), the Wenckebach cycle length and the AVERP and AVFRP (at two drive train cycle lengths), although the increases did not reach significance (Table 2). Finally, using sharp microelectrodes, intracellular action potentials were recorded from isolated right atrial preparations from a further 5 control and 6 PHT rats, because this technique allows the well-known electrical heterogeneity of the AV node[20] to be explored (Fig. 3). The preparations were paced from the region of the sinus node at 5 Hz. Normal AV node conduction was observed in 4 out of the 5 control preparations, whereas *abnormal* conduction was observed in 5 out of the 6 PHT preparations (Table S1). In PHT preparations, Fig. 3B shows an example of complete conduction block in the compact node (the action potentials show no correspondence to the stimulation artefacts and are spontaneous) and Fig. 3C shows a case of decremental conduction in the penetrating bundle. Taken together these data show evidence of AV node dysfunction in the PHT rat.

Remodelling of AV node

To understand the mechanisms underlying AV node dysfunction in PHT, the expression of ion channels, connexins, intracellular Ca^{2+}-handling proteins, ion pumps and exchangers and autonomic receptors was measured at the mRNA level using qPCR from 8 control and 8 PHT rats. Tissue was microdissected from four different regions of the AV node (transitional tissue, inferior nodal

extension, compact node and penetrating bundle – Fig. 4 inset[21] and Fig. S1 in Supplementary Material) as well as nearby atrial and ventricular muscle and total RNA was extracted from the different samples. Figs. 4-7 show the expression of many of the mRNA targets and Figs. S3-S6 show the expression of the remainder normalised to a housekeeper combination (B2M and PKG1). There are many significant differences in expression between different regions of the AV node, but for brevity are not discussed here. There are many significant differences in expression (generally downregulation) caused by PHT and these are considered below.

Downregulation of inward current carrying ion channels

In the AV node, inward current carrying ion channels play a role in diastolic depolarization, setting excitability and the upstroke and plateau of the action potential. HCN channels play an important role in pacemaking. HCN4 was the most abundant isoform and there was a trend of downregulation (significant in two regions) in the AV node in PHT (Fig. 4). $Na_v1.1$ is a subsidiary Na^+ channel involved in pacemaking and the action potential upstroke and again there was a trend of downregulation (significant in one region) in the AV node in PHT (Fig. 4). However, $Na_v1.5$ and $Na_v\beta1$ are responsible for the principal Na^+ channel in the heart and they were unaffected (Fig. 4). $Na_v1.8$ is responsible for the late Na^+ current;[22] its expression in the AV node was unaffected in PHT, but interestingly its expression level was high in the penetrating bundle (Fig. S3). $Ca_v1.2$ and $Ca_v1.3$ are L-type Ca^{2+} channels and $Ca_v3.1$ and $Ca_v3.2$ are T-type Ca^{2+} channels and all are involved in pacemaking and the action potential upstroke. There was a trend for all the Ca^{2+} channels to be downregulated (but only significant in some cases) in the AV node in PHT (Figs. 4 and S4). However, there were no changes in three Ca^{2+} channel accessory subunits ($Ca_v\alpha2\delta1$, $Ca_v\alpha2\delta2$ and $Ca_v\beta2$; Fig. S4). CLC-3 is a volume-regulated Cl^- channel[23] and it was significantly downregulated in the inferior nodal extension (Fig. S3). Another Cl^- channel, CLC-2, involved in pacemaking[23] was unaffected (Fig. S3). The downregulation of these ion channel transcripts in the AV node in PHT could potentially compromise AV node conduction by affecting excitability and the action potential upstroke.

Downregulation of outward current carrying ion channels

Voltage-gated K^+ channels play an important role in action potential repolarization. The voltage-gated K^+ channel subunits responsible for the transient outward K^+ current ($K_v1.4$, $K_v4.2$, $K_v4.3$, KChIP2) and delayed rectifier K^+ current ($K_v1.2$, $K_v1.5$, $K_v2.1$, ERG1, K_vLQT1, minK) tended to be downregulated (significantly in some cases) in the AV node in PHT (Figs. 5 and S3). There were three significant decreases in inward rectifier K^+ channels in the AV node in PHT: $K_{ir}3.1$ (subunit of ACh-activated K^+ channel) in the transitional tissue, $K_{ir}3.4$ (another subunit of ACh-activated K^+ channel) in the inferior nodal extension and $K_{ir}6.2$ (subunit of ATP-sensitive K^+ channel) in the transitional tissue (Fig. 6). The twin pore K^+ channel, TWIK1, was significantly downregulated in the inferior nodal extension in the AV node in PHT (Fig. 6). The downregulation of the K^+ channels is expected to prolong the AV node action potential although such an effect would be countered by the downregulation of inward current carrying ion channels.

Downregulation of intracellular Ca^{2+}-handling molecules

Intracellular Ca^{2+} plays an important role in pacemaking and conduction in the AV node.[24,25] Expression of many intracellular Ca^{2+}-handling molecules was affected in PHT. There tended to be a downregulation of NCX1 (Na^+-Ca^{2+} exchanger) in the AV node in PHT, but this was not significant (Fig. 7). There was a tendency for RyR2 (the Ca^{2+} release channel of the sarcoplasmic reticulum - SR) to be downregulated in most tissues in PHT and it was significantly downregulated in the inferior nodal extension (Fig. 7). Although expression of SERCA2 in the AV node was not affected in PHT, two regulators of SERCA2 (phospholamban and sarcolipin) were significantly downregulated in much of the AV node (Fig. 7). Two other Ca^{2+}-handling molecules, calsequestrin 2 and PMCA1, were unaffected (Figs. 7 and S3). The downregulation of RyR2 could potentially slow AV node conduction.

Downregulation of other transcripts

In PHT, there was a trend of downregulation of the $\alpha2$ and $\alpha3$ subunits of the Na^+-K^+ pump throughout the AV node (significantly in some cases; Fig. S5). However, the $\alpha1$ and $\beta1$ subunits

were unchanged (Fig. S5). The Na^+-H^+ exchanger (NHE1) was significantly upregulated in the inferior nodal extension in PHT (Fig. S3). Connexins are responsible for electrical coupling between myocytes and therefore are an important determinant of conduction velocity of the action potential. No changes were seen in Cx40, Cx43 and Cx45 in any of the nodal tissues (Fig. 7). However, Cx30.2 has been suggested to play a key role in nodal tissues[26] and it was significantly downregulated in both the transitional tissue and inferior nodal extension in PHT (Fig. 7). The AV node is controlled by the autonomic nervous system. Although there were no changes in the M2 muscarinic and A1 adenosine receptors in the AV node in PHT, there were changes in adrenergic receptors: there was a significant downregulation in the α1a/1c adrenergic receptor in the inferior nodal extension and importantly there was a significant downregulation of the β1 receptor (the most important adrenergic receptor) in the inferior nodal extension (Fig. S6). There were no significant changes in two other adrenergic receptors (α1b and β2; Fig. S6). The downregulation of the β1 adrenergic receptor could negatively impact AV node conduction.

Remodelling predicts heart block

The significant changes in transcripts in the AV node in PHT in the present study are summarised in Tables S2 and S3. Biophysically-detailed action potential models have been used to predict *possible* changes in electrical activity based on changes in ion channel transcripts – ionic conductances are scaled depending on changes in mRNA (Supplementary Material). This should be viewed as a form of bioinformatics. Based on a biophysically-detailed one-dimensional (1D) model of the conduction pathway from the atrium through the AV node and Purkinje fibres to the ventricle,[27] Fig. 8 shows the predicted effects of PHT-induced ion channel remodelling; the assumed changes in ionic conductances (based on expression of corresponding mRNAs) are shown in Table S11. In control conditions, the action potential is predicted to conduct from the atrium to the ventricle (Fig. 8A) and the conduction velocity (Fig. 8B) and action potential waveform (Fig. 8C) in the different tissues are as expected. However in PHT, conduction is predicted to fail in the compact node (heart block; Fig. 8) consistent with Figs. 2 and 3. Of the changes in ion channels in PHT, the computer

modelling predicts that the downregulation of the L-type Ca^{2+} channels, $Ca_v1.2$ and $Ca_v1.3$, is the most important. The expected downregulation of $I_{Ca,L}$ in the N region alone is sufficient to cause heart block (data not shown).

Discussion

This study is the first to demonstrate widespread downregulation of the ion channel transcriptome in the AV node in response to a disease process. Previously, AV node disease has been commonly attributed to idiopathic fibrosis and sclerosis.[e.g.28] However, there are other recent data pointing to the importance of ion channels in normal AV conduction. A genome wide association study has demonstrated several loci that are associated with a prolonged PR interval, including genes for ion channels and developmental genes known to be important for the patterning of ion channels during embryogenesis.[29] There is also a recognition that several disease-causing ion channel mutations that have been characterised as causing Brugada syndrome and long-QT syndrome are also associated with conduction system disturbances and heart block.[19] In addition to these findings in patients, gene knockout studies in mice have pointed to the importance of several ion channels including voltage-dependent Ca^{2+} channels[e.g.30] and HCN4[31] in maintaining normal AV conduction.

Dysfunction and remodelling of AV node in PHT

There was evidence of dysfunction of the AV node in the PHT rats: in the Langendorff-perfused heart, there was evidence of an increase in the AVERP, AVFRP and Wenckebach cycle length and, in the isolated AV node, there was a 50% incidence of complete heart block (Fig. 3). In one case, in which a PHT rat died with a telemetry system fitted, it died of heart block (Fig. 1C) and this is consistent with earlier telemetric studies;[10,11] for example, Chi *et al.*[11] reported that ~38% of PHT (monocrotaline-injected) rats die of heart block. There was a widespread downregulation in the ion channel transcriptome in the AV node in PHT (Tables S2 and S3). AV node conduction will be potentially slowed by the downregulation of many of the transcripts and computer modelling confirmed that if the changes in mRNA are translated into changes in function they will result in heart block (Fig. 8). The potential role played by the downregulation of some transcripts will be briefly discussed.

Primary role for Ca^{2+} channels

The upstroke and conduction of the action potential of the AV node is known to be dependent on L-type Ca^{2+} channels. For example, knockout of either $Ca_v1.2$ and $Ca_v1.3$ has been reported to slow or block AV node conduction.[32,33] A downregulation of $Ca_v1.2$ and $Ca_v1.3$ was observed in the AV node in PHT (Fig. 4) and the computer modelling predicts that the expected decrease in L-type Ca^{2+} current alone is sufficient to cause heart block. We suggest that this is the primary cause of AV node dysfunction in PHT.

The T-type Ca^{2+} channels, $Ca_v3.1$ and $Ca_v3.2$, also tended to decrease (Figs. 4 and S4) and knockout of $Ca_v3.1$ at least has been shown to slow AV node conduction.[30] RyR2 was significantly downregulated in the AV node in PHT (Fig. 7). RyR2 is an important part of the Ca^{2+} clock. The 'Ca^{2+} clock' as well as the 'membrane clock' (the principal component of which is the funny current, I_f) controls pacemaking in the sinus and AV nodes.[24] However, there is also evidence that it controls AV node conduction: Saeed *et al.*[25] have shown that incapacitating RyR2 and the Ca^{2+} clock by application of ryanodine slows AV node conduction. The Ca^{2+} clock could control AV node conduction by affecting excitability and, therefore, the downregulation of RyR2 in PHT may be important. Further components of the Ca^{2+} clock tended to be downregulated in the AV node in PHT (Fig. 7), markedly in the case of phospholamban and sarcolipin; the consequences of these changes for AV node conduction are unknown.

Role for downregulation of HCN4?

Downregulation of the HCN4 channel in the AV node was observed in PHT (Fig. 4; see also Fig. S8). HCN channels and I_f (inward current during diastole that is responsible for phase 4 depolarization) have mainly been considered in relation to sinus node pacemaking. Indeed an I_f blocking drug, ivabradine, is used clinically to reduce sinus rate. Initial studies on a small number of patients demonstrated no effects on the AV node and therefore subsequent larger studies have not investigated the effects of ivabradine on the AV node.[e.g.34] However, there are several recent studies that suggest that I_f may play a significant role in AV node conduction. This study has demonstrated

high levels of HCN4 in the AV node (Fig. 4). There is also functional evidence that I_f plays a role in AV node conduction: although ivabradine was not shown to have an effect on the human AV node, another I_f blocking agent, zatebradine, has been shown to increase the AH interval, AVERP and Wenckebach cycle length in humans.[35] Ivabradine has also been shown to slow the ventricular response to atrial fibrillation in dogs with the mechanism thought to be specific to I_f blockade within the AV node slowing conduction and not a direct effect of I_f blockade on the atrium.[36] Inducible cardiac specific knockout of HCN4 in mice is lethal because of the development of complete heart block.[31] Saeed *et al.*[25] have shown that in young rats I_f block significantly prolongs the AH interval, AVERP and Wenckebach cycle length. Downregulation of I_f could slow AV node conduction by decreasing excitability of the cell.[37]

Role for other factors?

A downregulation of various K^+ channels was observed in the AV node in PHT (Figs. 5 and 6). This is not surprising, because in the ventricles a downregulation of K^+ channels has been shown in a number of different disease models including PHT.[38] In the ventricles, the downregulation leads to a prolongation of the action potential.[38] In the present study, it has not been highlighted, but many K^+ channels were downregulated in both the atrial and ventricular working myocardium (Figs. 5, 6 and S3) and the functional experiments demonstrated an increased VERP and suggested an increased AERP, which is consistent with an increase in action potential duration. The downregulation of K^+ channels in the AV node could explain the observed increase in AVERP, AVFRP and Wenckebach cycle length in PHT (Fig. 2). In the transitional tissue at least, the computer modelling predicts a prolongation of the AV node action potential in PHT (Fig. 8). Regan *et al.*[39] observed that selective pharmacological block of ERG ($I_{K,r}$) and K_vLQT1 ($I_{K,s}$) both cause a prolonged AH interval and AVERP in rats. Although ERG and K_vLQT1 were unaffected by PHT (Fig. 5), this demonstrates that K^+ channels are able to affect AV node conduction and refractoriness. Recently, Mesirca *et al.*[40] reported that ablation of the ACh-activated K^+ current (carried by $K_{ir}3.1$ and $K_{ir}3.4$) relieves the heart block in $Ca_v1.3$ knockout mice. In PHT, $K_{ir}3.1$ and

$K_{ir}3.4$ tended to be downregulated in PHT and this could be a compensatory mechanism. Changes in K^+ channels could potentially alter the membrane potential during diastole and this would have indirect consequences, for example for the Na^+ current. The only connexin that was significantly affected within the nodal tissue was Cx30.2, which was downregulated (Fig. 7). However, paradoxically, knockout of the very low conductance Cx30.2 leads to an increased conduction velocity across the AV node.[41]

Cardiac sympatholysis

Activation of the sympathetic nervous system and an increase in plasma norepinephrine levels is a feature of heart failure.[42] In keeping with this, Leineweber *et al.*[43] showed that, in the monocrotaline-injected rat, plasma norepinephrine levels are markedly increased. The activation of the sympathetic nervous system can support the failing heart (although it can also be detrimental to the heart and cause hypertrophy for example).[42] In the present study, whereas AV node function was generally normal *in vivo* (Table 1), AV node function was worse in the Langendorff-perfused heart (AVERP and AVFRP were significantly longer; Table 2) and it was worse again in the isolated right atrial preparation (when conduction block was frequently observed; Figs. 2 and 3 and Tables 2 and S1). This is consistent with dysfunction of the AV node in PHT and *in vivo* the failing AV node being supported by the activation of the sympathetic nervous system.

In heart failure, the elevated norepinephrine levels are known to result in downregulation of β-receptors as a result of desensitization.[42] In the monocrotaline-injected rat, Leineweber *et al.*[43] showed that there is a downregulation of β-receptors at the protein level and a diminished responsiveness to β-stimulation. The data from the present study are consistent with this. In the rat, of the β1- and β2-receptors, the β1-receptor is the dominant isoform[43] and the same is true in the present study at the mRNA level (Fig. S6). In the present study, there tended to be a downregulation of β-receptors in the PHT rats (although the downregulation was only significant in some regions; Fig. S6). Interestingly, in the present study, there was also a downregulation of α-receptors at the mRNA level in some regions (Fig. S6); Leineweber *et al.*[43] also reported a downregulation. In a

pilot experiment, sympathetic nerve fibres in the AV node were immunolabelled using an antibody to neurofilament 150;[44] dense innervation was observed, but there was no marked change in PHT (Fig. S7). The consequences of these changes can only be speculated on. The downregulation of β-receptors in PHT could contribute to failure of the AV node *in vivo* (because activation of the sympathetic nervous system would no longer be able to support the failing AV node).

Clinical implications

Heart block is a common condition in both PHT and the general population and is the indication for over half of implanted pacemakers.[45] AV node disease has typically been attributed to fibrosis, but this study shows that this is not necessarily the case. This study shows that in PHT it is more likely to be the result of remodelling of the ion channel transcriptome. In this respect, the AV node is no different from the rest of the heart – in heart disease, there is a well-known remodelling of the ion channel transcriptome in the sinus node and working myocardium. Recognition of the causes of AV node disease is the first step to developing new treatments.

Further discussion of the findings can be found in the Supplementary Material.

References

1. Bossone E, Paciocco G, Iarussi D, Agretto A, Iacono A, Gillespie BW and Rubenfire M. The prognostic role of the ECG in primary pulmonary hypertension. *Chest*. 2002;121:513-518.
2. Kanemoto N and Sasamoto H. Arrhythmias in primary pulmonary hypertension. *Jpn Heart J*. 1979;20:765-775.
3. Tongers J, Schwerdtfeger B, Klein G, Kempf T, Schaefer A, Knapp JM, Niehaus M, Korte T and Hoeper MM. Incidence and clinical relevance of supraventricular tachyarrhythmias in pulmonary hypertension. *Am Heart J*. 2007;153:127-32.
4. Ruiz-Cano MJ, Gonzalez-Mansilla A, Escribano P, Delgado J, Arribas F, Torres J, Flox A, Riva M, Gomez MA and Saenz C. Clinical implications of supraventricular arrhythmias in patients with severe pulmonary arterial hypertension. *Int J Cardiol*. 2011;146:105-6.
5. Aro AL, Anttonen O, Kerola T, Junttila MJ, Tikkanen JT, Rissanen HA, Reunanen A and Huikuri HV. Prognostic significance of prolonged PR interval in the general population. *Eur Heart J*. 2014;35:123-9.
6. Laks L, Lehrhaft B, Grunstein RR and Sullivan CE. Pulmonary hypertension in obstructive sleep apnoea. *Eur Respir J*. 1995;8:537-41.
7. Koehler U, Fus E, Grimm W, Pankow W, Schafer H, Stammnitz A and Peter JH. Heart block in patients with obstructive sleep apnoea: pathogenetic factors and effects of treatment. *Eur Respir J*. 1998;11:434-9.
8. Uzzaman M, Honjo H, Takagishi Y, Emdad L, Magee AI, Severs NJ and Kodama I. Remodeling of gap junctional coupling in hypertrophied right ventricles of rats with monocrotaline-induced pulmonary hypertension. *Circ Res*. 2000;86:871-878.
9. Stenmark KR, Meyrick B, Galie N, Mooi WJ and McMurtry IF. Animal models of pulmonary arterial hypertension: the hope for etiological discovery and pharmacological cure. *Am J Physiol*. 2009;297:L1013-32.
10. Watkinson WP, Campen MJ and Costa DL. Cardiac arrhythmia induction after exposure to residual oil fly ash particles in a rodent model of pulmonary hypertension. *Toxicol Sci*. 1998;41:209-16.

11. Chi L, Liles J, Arolfo M, Oliver J, Dhalla A and Belardinelli L. Direct evidence of unprovoked arrhythmias in telemetered, conscious rats with chronic pulmonary artery hypertension. *Am J Resp Crit Care*. 2013;187:A4648.

12. Benoist D, Stones R, Drinkhill MJ, Benson AP, Yang Z, Cassan C, Gilbert SH, Saint DA, Cazorla O, Steele DS, Bernus O and White E. Cardiac arrhythmia mechanisms in rats with heart failure induced by pulmonary hypertension. *Am J Physiol-Heart C*. 2012;302:H2381-95.

13. Katagiri F. Multiple tests correction, false discovery rate and q value. *Physiology News*. 2009;77:35-38.

14. Rothman KJ. No adjustments are needed for multiple comparisons. *Epidemiology*. 1990;1:43-6.

15. Myers SA, Eriksson N, Burow R, Wang SC and Muscat GE. Beta-adrenergic signaling regulates NR4A nuclear receptor and metabolic gene expression in multiple tissues. *Mol Cell Endocrinol*. 2009;309:101-8.

16. Yanni J, Tellez JO, Maczewski M, Mackiewicz U, Beresewicz A, Billeter R, Dobrzynski H and Boyett MR. Changes in ion channel gene expression underlying heart failure-induced sinoatrial node dysfunction. *Circulation: Heart Failure*. 2011;4:496-508.

17. Koskenvuo JW, Mirsky R, Zhang Y, Angeli FS, Jahn S, Alastalo TP, Schiller NB, Boyle AJ, Chatterjee K, De Marco T and Yeghiazarians Y. A comparison of echocardiography to invasive measurement in the evaluation of pulmonary arterial hypertension in a rat model. *International Journal of Cardiovascular Imaging*. 2010;26:509-18.

18. Urboniene D, Haber I, Fang YH, Thenappan T and Archer SL. Validation of high-resolution echocardiography and magnetic resonance imaging vs. high-fidelity catheterization in experimental pulmonary hypertension. *Am J Physiol-Lung C*. 2010;299:L401-12.

19. Dobrzynski H, Anderson RH, Atkinson A, Borbas Z, D'Souza A, Fraser JF, Inada S, Logantha SJRJ, Monfredi O, Morris GM, Moorman AFM, Nikolaidou T, Schneider H, Szuts V, Temple IP, Yanni J and Boyett MR. Structure, function and clinical relevance of the cardiac conduction system, including the atrioventricular ring and outflow tract tissues. *Pharmacol Therapeut*. 2013;139:260-288.

20. Billette J. Atrioventricular nodal activation during periodic premature stimulation of the atrium. *Am J Physiol*. 1987;252:H163-H177.

21. Greener ID, Tellez JO, Dobrzynski H, Yamamoto M, Graham GM, Billeter R and Boyett MR. Ion channel transcript expression at the rabbit atrioventricular conduction axis. *Circulation: Arrhythmia and Electrophysiology*. 2009;2:305-315.

22. Yang T, Atack TC, Stroud DM, Zhang W, Hall L and Roden DM. Blocking Scn10a channels in heart reduces late sodium current and is antiarrhythmic. *Circ Res*. 2012;111:322-32.

23. Duan D. Phenomics of cardiac chloride channels: the systematic study of chloride channel function in the heart. *J Physiol*. 2009;587:2163-77.

24. Cheng H, Smith GL, Hancox JC and Orchard CH. Inhibition of spontaneous activity of rabbit atrioventricular node cells by KB-R7943 and inhibitors of sarcoplasmic reticulum Ca^{2+} ATPase. *Cell Calcium*. 2011;49:56-65.

25. Saeed Y, Temple IP, Borbas Z, Atkinson A, Yanni J, Boyett MR, Garratt C and Dobrzynski H. Do major ion channels of pacemaker clock play a role in AV nodal conduction in young and old rats? *Eur Heart J*. 2015;36 (Abstract Supplement):1121.

26. Kreuzberg MM, Schrickel JW, Ghanem A, Kim JS, Degen J, Janssen-Bienhold U, Lewalter T, Tiemann K and Willecke K. Connexin30.2 containing gap junction channels decelerate impulse propagation through the atrioventricular node. *P Natl Acad Sci USA*. 2006;103:5959-64.

27. Inada S, Hancox JC, Zhang H and Boyett MR. One-dimensional mathematical model of the atrioventricular node including atrio-nodal, nodal, and nodal-his cells. *Biophys J*. 2009;97:2117-2127.

28. Bailey S, Burkhardt JD and Bhargava M. Bradycardia. In: A. Natale and F. Marchlinski, eds. *Handbook of Cardiac Electrophysiology*: CRC Press; 2007: 51-60.

29. Pfeufer A, van Noord C, Marciante KD, Arking DE, Larson MG, Smith AV, Tarasov KV, Muller M, Sotoodehnia N, Sinner MF, Verwoert GC, Li M, Kao WH, Kottgen A, Coresh J, Bis JC, Psaty BM, Rice K, Rotter JI, Rivadeneira F, Hofman A, Kors JA, Stricker BH, Uitterlinden AG, van Duijn CM, Beckmann BM, Sauter W, Gieger C, Lubitz SA, Newton-Cheh C, Wang TJ, Magnani JW, Schnabel RB, Chung MK, Barnard J, Smith JD, Van Wagoner DR, Vasan RS, Aspelund T, Eiriksdottir G, Harris TB, Launer LJ, Najjar SS, Lakatta E, Schlessinger D, Uda M, Abecasis GR, Muller-Myhsok B, Ehret GB, Boerwinkle E, Chakravarti A, Soliman EZ, Lunetta KL, Perz S, Wichmann HE,

Meitinger T, Levy D, Gudnason V, Ellinor PT, Sanna S, Kaab S, Witteman JC, Alonso A, Benjamin EJ and Heckbert SR. Genome-wide association study of PR interval. *Nat Genet*. 2010;42:153-9.

30. Marger L, Mesirca P, Alig J, Torrente A, Dubel S, Engeland B, Kanani S, Fontanaud P, Striessnig J, Shin HS, Isbrandt D, Ehmke H, Nargeot J and Mangoni ME. Functional roles of $Ca_v1.3$, $Ca_v3.1$ and HCN channels in automaticity of mouse atrioventricular cells: insights into the atrioventricular pacemaker mechanism. *Channels*. 2011;5:251-61.

31. Baruscotti M, Bucchi A, Viscomi C, Mandelli G, Consalez G, Gnecchi-Rusconi T, Montano N, Casali KR, Micheloni S, Barbuti A and DiFrancesco D. Deep bradycardia and heart block caused by inducible cardiac-specific knockout of the pacemaker channel gene Hcn4. *P Natl Acad Sci USA*. 2011;108:1705-10.

32. Foell JD, Best JM, Lei M, Balijepalli RC, Molkentin JD, Powers PA, McKinnon D and Kamp TJ. Targeted loss of cardiac L-type Ca^{2+} $Ca_v1.2$ Channels in adult mouse causes sinus node dysfunction, AV block and supraventricular tachycardias. *Circulation*. 2008;118:S-436.

33. Matthes J, Yildirim L, Wietzorrek G, Reimer D, Striessnig J and Herzig S. Disturbed atrio-ventricular conduction and normal contractile function in isolated hearts from Cav1.3-knockout mice. *N-S Arch Pharmacol*. 2004;369:554-562.

34. Swedberg K, Komajda M, Bohm M, Borer JS, Ford I and Tavazzi L. Rationale and design of a randomized, double-blind, placebo-controlled outcome trial of ivabradine in chronic heart failure: the Systolic Heart Failure Treatment with the I_f Inhibitor Ivabradine Trial (SHIFT). *Eur J Heart Fail*. 2010;12:75-81.

35. Chiamvimonvat V, Newman D, Tang A, Green M, Mitchell J, Wulffhart Z and Dorian P. A double-blind placebo-controlled evaluation of the human electrophysiologic effects of zatebradine, a sinus node inhibitor. *J Cardiovasc Pharm*. 1998;32:516-20.

36. Verrier RL, Sobrado MF, Pagotto VP, Kanas AF, Machado AD, Varone BB, Sobrado LF, Nearing BD, Zeng D and Belardinelli L. Inhibition of I_f in the atrioventricular node as a mechanism for dronedarone's reduction in ventricular rate during atrial fibrillation. *Heart Rhythm*. 2013;10:1692-7.

37. Li J, Temple IP and Boyett MR. Theoretical study of the role of the funny current (I_f) and the background inward current (I_b) in atrioventricular nodal conduction. *Computing in Cardiology*. 2014; 41:865-868.

38. Benoist D, Stones R, Drinkhill M, Bernus O and White E. Arrhythmogenic substrate in hearts of rats with monocrotaline-induced pulmonary hypertension and right ventricular hypertrophy. *Am J Physiol*. 2011;300:H2230-H2237.

39. Regan CP, Cresswell HK, Zhang R and Lynch JJ. Novel method to assess cardiac electrophysiology in the rat: characterization of standard ion channel blockers. *J Cardiovasc Pharm*. 2005;46:68-75.

40. Mesirca P, Bidaud I, Briec F, Evain S, Torrente AG, Le Quang K, Leoni AL, Baudot M, Marger L, Chung You Chong A, Nargeot J, Striessnig J, Wickman K, Charpentier F and Mangoni ME. G protein-gated I_{KACh} channels as therapeutic targets for treatment of sick sinus syndrome and heart block. *P Natl Acad Sci USA*. 2016;113:E932-41.

41. Temple IP, Inada S, Dobrzynski H and Boyett MR. Connexins and the atrioventricular node. *Heart Rhythm*. 2013;10:297-304.

42. Liang CS. Sympatholysis and cardiac sympathetic nerve function in the treatment of congestive heart failure. *J Am Coll Cardiol*. 2003;42:549-51.

43. Leineweber K, Seyfarth T, Abraham G, Gerbershagen HP, Heinroth-Hoffmann I, Ponicke K and Brodde OE. Cardiac beta-adrenoceptor changes in monocrotaline-treated rats: differences between membrane preparations from whole ventricles and isolated ventricular cardiomyocytes. *J Cardiovasc Pharm*. 2003;41:333-42.

44. Trojanowski JQ, Walkenstein N and Lee VM. Expression of neurofilament subunits in neurons of the central and peripheral nervous system: an immunohistochemical study with monoclonal antibodies. *J Neurosci*. 1986;6:650-60.

45. Uslan DZ, Tleyjeh IM, Baddour LM, Friedman PA, Jenkins SM, St Sauver JL and Hayes DL. Temporal trends in permanent pacemaker implantation: a population-based study. *Am Heart J*. 2008;155:896-903.

Sources of funding

Work undertaken with support of a Clinical Research Fellowship (FS/10/69/28495) and a programme grant (RG/11/18/29257) from the British Heart Foundation.

Disclosures

None.

Table 1. Body, heart and lung weights at day 0, day 21 and day of sacrifice and echocardiography and ECG parameters on day of sacrifice. Data are presented as mean±SEM. Differences between monocrotaline-injected and control rats assessed by Student's *t*-test; *significantly different from control data. LV, left ventricle; PAAD, pulmonary artery acceleration time; PAD, pulmonary artery deceleration; PVmax, maximum pulmonary artery velocity; RV, right ventricle.

	Control rats	**PHT rats**	**P value**
Body, heart and lung weights			
Body weight at day 0 (g; n=8/8)	208±9	208±5	0.9897
Body weight at day 21 (g; n=8/8)	299±13	277±7	0.1573
Body weight on day of termination (g; n=8/8)	308±15	270±8*	0.0446
Heart weight (g; n=6/8)	1.6±0.1	1.9± 0.1*	0.0239
Heart:body weight ratio (n=6/8)	0.0050±0.0004	0.0070±0.0003*	0.0010
Lung weight (g; n=8/8)	1.4±0.1	2.7±0.2*	<0.0001
Lung:body weight ratio (n=8/8)	0.0050±0.0003	0.0100±0.0009*	0.0001
Echocardiography parameters			
LV septal wall thickness, diastole (cm; n=8/8)	0.15±0.01	0.18±0.01	0.1978
LV internal diameter, diastole (cm; n=8/8)	0.71±0.03	0.44±0.05*	0.0002
LV posterior wall, diastole thickness (cm; n=8/8)	0.18±0.01	0.20±0.01	0.3874
LV septal wall thickness, systole (cm; n=8/8)	0.26±0.02	0.30±0.02	0.1275
LV internal diameter, systole (cm; n=8/8)	0.36±0.03	0.17±0.03*	0.0004
LV posterior wall, systole thickness (cm; n=8/8)	0.27±0.01	0.29±0.02	0.3719
PAAT (ms; n=8/8)	33.0±3.6	14.3±0.6*	0.0001
PAD (m/s; n=8/8)	14.9±1.7	33.6±3.5*	0.0003
PVmax (m/s; n=8/8)	1.09±0.05	0.70±0.05*	<0.0001
RV wall thickness, diastole (cm; n=8/8)	0.09±0.01	0.14±0.01*	<0.0001
RV internal dimension, diastole (cm; n=8/8)	0.27±0.02	0.38±0.05	0.0598
RV wall thickness, systole (cm; n=8/8)	0.13±0.01	0.16±0.01*	0.0375
RV internal dimension, systole (cm; n=8/8)	0.12±0.02	0.25±0.04*	0.0065
RV fractional shortening (%; n=8/8)	54.4±4.9	34.4±5.1*	0.0131
ECG parameters			
RR interval (ms; n=27/28)	145±2	158±2*	<0.0001
PR interval (ms; n=27/28)	46.1±0.7	45.8±0.7	0.7269
QRS duration (ms; n=27/28)	15.5±0.5	14.7±0.4	0.2309
QT interval (ms; n=27/27)	52±2	103±3*	<0.0001
QTc interval (ms; n=27/27)	136.7±4.1	259.3±6.9*	<0.0001

Table 2. Electrical properties of Langendorff-perfused heart and isolated AV node preparation from control and PHT rats. Data are presented as mean±SEM. Differences between PHT and control rats assessed by Student's *t*-test; Fisher's exact test was used to compare incidences of complete heart block; *significantly different from control data. AERP, atrial effective refractory period; AVERP, AV node effective refractory period; AVFRP, AV node functional refractory period; VERP, ventricular effective refractory period.

	Control rats	**PHT rats**	**P value**
Isolated Langendorff-perfused heart			
RR interval (ms; n=9/11)	237±8	244±14	0.6556
PR interval (ms; n=9/11)	43±2	44±2	0.6922
QT interval (ms; n=9/11)	56±5	135±10*	<0.0001
QTc interval (ms; n=9/11)	116±10	275±18*	<0.0001
QRS duration (ms; n=9/11)	13±1	16±3	0.3813
AERP (ms; n=9/9)	34±2	43±5	0.1508
Wenckebach cycle length (ms; n=10/11)	111±3	117±3	0.1640
AVERP (ms; n=10/10)	88±1	94±3*	0.0364
AVFRP (ms; n=10/10)	115±2	122±2*	0.0122
VERP (ms; n=6/4)	40±3	98±11*	0.0003
Isolated right atrium-AV node preparation			
RR interval (ms; n=9/11)	216±10	212±7	0.7143
AH interval (ms; n=10/6)	41±5	53±6	0.1579
Wenckebach cycle length (ms; n=9/5)	129±7	139±11	0.4932
AVERP (200 ms cycle length; n=5/4)	110±13	114±13	0.8113
AVERP (150 ms cycle length; n=6/2)	95±4	102±15	0.5008
AVFRP (200 ms cycle length; n=2/4)	133±1	138±11	0.7759
AVFRP (150 ms cycle length; n=7/2)	117±5	127±6	0.3517
Incidence of complete heart block (%; n=10/12)	0%	50%*	0.015

Figure legends

Fig. 1. A and B, echocardiography images (on day 23 following monocrotaline injection) showing development of PHT. A, parasternal short axis view from control (Ai) and monocrotaline-injected (Aii) rats. The left and right ventricles (LV and RV) are identified by dotted lines (not possible to identify right ventricle in control rat). B, pulmonary velocity profile from control (Bi) and monocrotaline-injected (Bii) rats. Measurement of pulmonary artery acceleration time (PAAT) and pulmonary artery deceleration (PAD) shown. C, death of rat with PHT caused by complete heart block 28 days following monocrotaline injection. ECGs recorded by telemetry at different times during final 21 min shown. Ratio of atrial to ventricular beats shown in blue. ECGs shown on different time bases (1 s time marks shown). Y-axis shows 0.2 mV increments. CHB, complete heart block.

Fig. 2. Impaired AV node conduction in PHT rats. All data collected on day of termination. A (left), mean (+SEM) Wenckebach cycle length (WCL), AVERP and AVFRP in control (black bars) and PHT (red bars) rats (n=10). Recordings made from Langendorff-perfused heart. *P<0.05 (Student's t test). A (right), typical AV node conduction curves from control and PHT rats showing measurement of AVERP and AVFRP. B, significant correlation between AVERP and AVFRP and Wenckebach cycle length. Each point corresponds to different rat, control (black) or PHT (red). Data are fit by linear regression (AVERP, R^2=0.63, P<0.001; AVFRP, R^2=0.71, P<0.0001). C, demonstration of complete heart block in PHT rat. Extracellular potential recordings from region of His bundle of control (top trace) and PHT (bottom trace) rats shown. Recordings made from isolated AV node. Atrial (labelled A and marked with green arrow) as well as His bundle (labelled H and marked with red arrow) signals recorded.

Fig. 3. Heart block in PHT rats explored further. A, example of AV node preparation used for intracellular action potential recording. Tissue was paced at 5 Hz at level of sinus node. B, intracellular action potentials recorded from compact node showing normal 1:1 conduction in control preparation and complete heart block (as well as ectopic action potentials) in PHT preparation. Sharp deflections, stimulation artefacts. C, intracellular action potentials recorded along AV conduction axis (transitional tissue, inferior nodal extension/compact node and penetrating bundle) showing normal conduction in control preparation and decremental conduction in penetrating bundle in PHT preparation.

Fig. 4. Expression of mRNA for ion channels carrying inward current. In this and similar figures: expression shown in atrial muscle (A; A), transitional tissue (B; TT), inferior nodal extension (C; INE), compact node (D; CN), penetrating bundle (E; PB) and ventricular muscle (F; V) from control (black bars) and PHT (red bars) rats; means (+SEM) shown (n=6-8); bars and asterisks indicate significant differences between control and PHT rats as assessed by the limma test (FDR-corrected $P<0.2$, i.e. 20%); and, for the control tissues only, letters indicate a significant difference from the appropriately lettered region (lower case letters, FDR-corrected $P<0.2$, i.e. 20%; upper case letters, FDR-corrected $P<0.05$, i.e. 5%). Inset, schematic diagram of AV node (from Greener *et al.*[21]). CFB, central fibrous body; CS, coronary sinus; IVC, inferior vena cava; FO, fossa ovalis; TV, tricuspid valve.

Fig. 5. Expression of mRNA for voltage-gated K^+ channels.

Fig. 6. Expression of mRNA for inward rectifier K^+ channels.

Fig. 7. Expression of mRNA for Ca^{2+}-handling molecules and connexins.

Fig. 8. Remodelling of AV node predicts heart block in PHT. A, simulated conduction along AV conduction axis under control conditions (top) and in PHT (bottom). Propagation of five consecutive action potentials shown. Membrane potential (colour coded) is shown as a function of time and distance. B, computed conduction velocity (CV) along AV conduction axis under control conditions and in PHT. C, computed action potential profiles along AV conduction axis under control conditions and in PHT.

Fig. 1

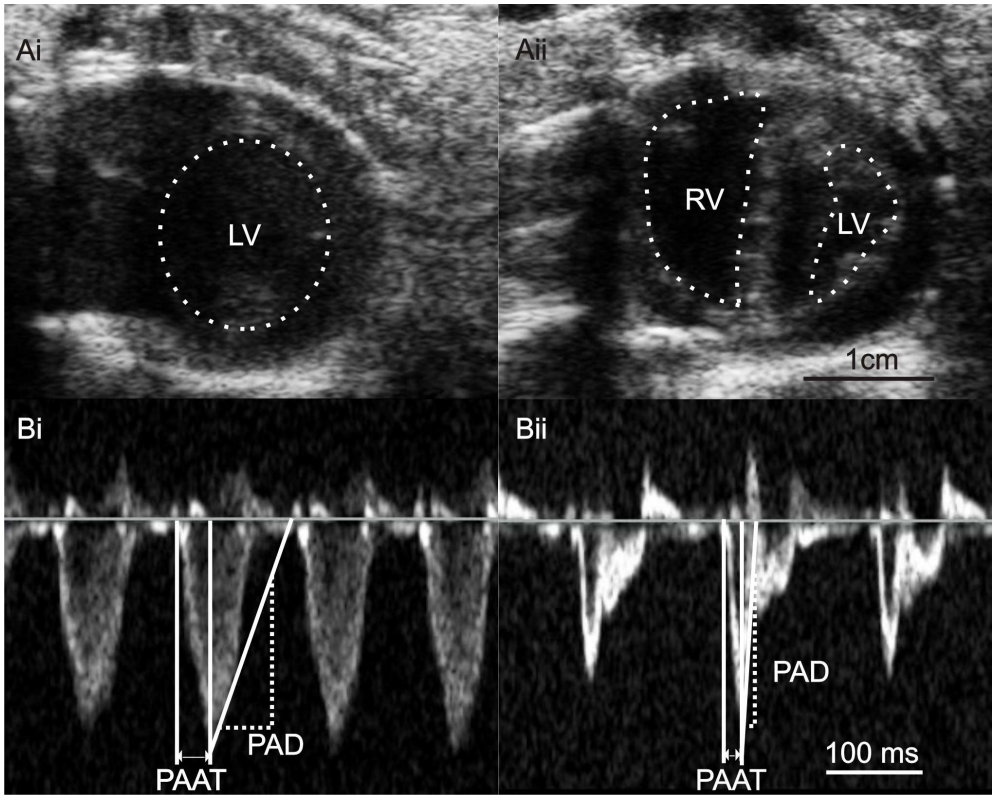
Ai
LV
Aii
RV
LV
1cm
Bi
PAD
PAAT
Bii
PAD
PAAT
100 ms

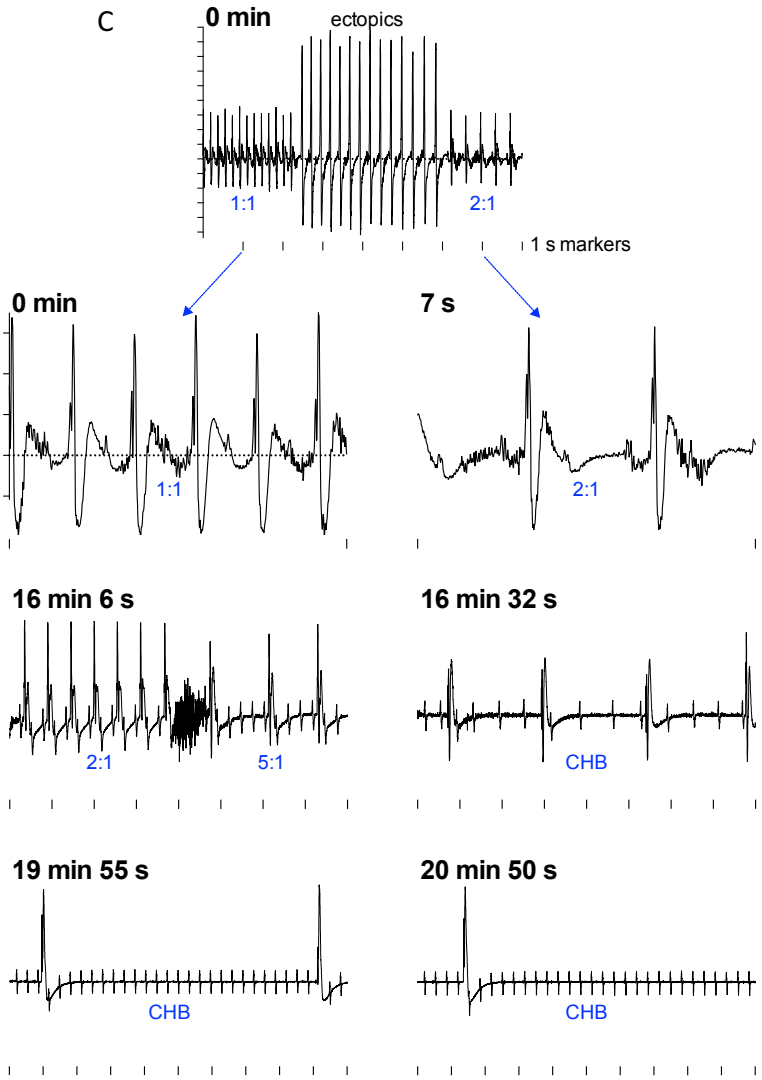
C
0 min
ectopics
1:1
2:1
1 s markers
0 min
1:1
7 s
2:1
16 min 6 s
2:1
5:1
16 min 32 s
CHB
19 min 55 s
CHB
20 min 50 s
CHB

Fig. 2

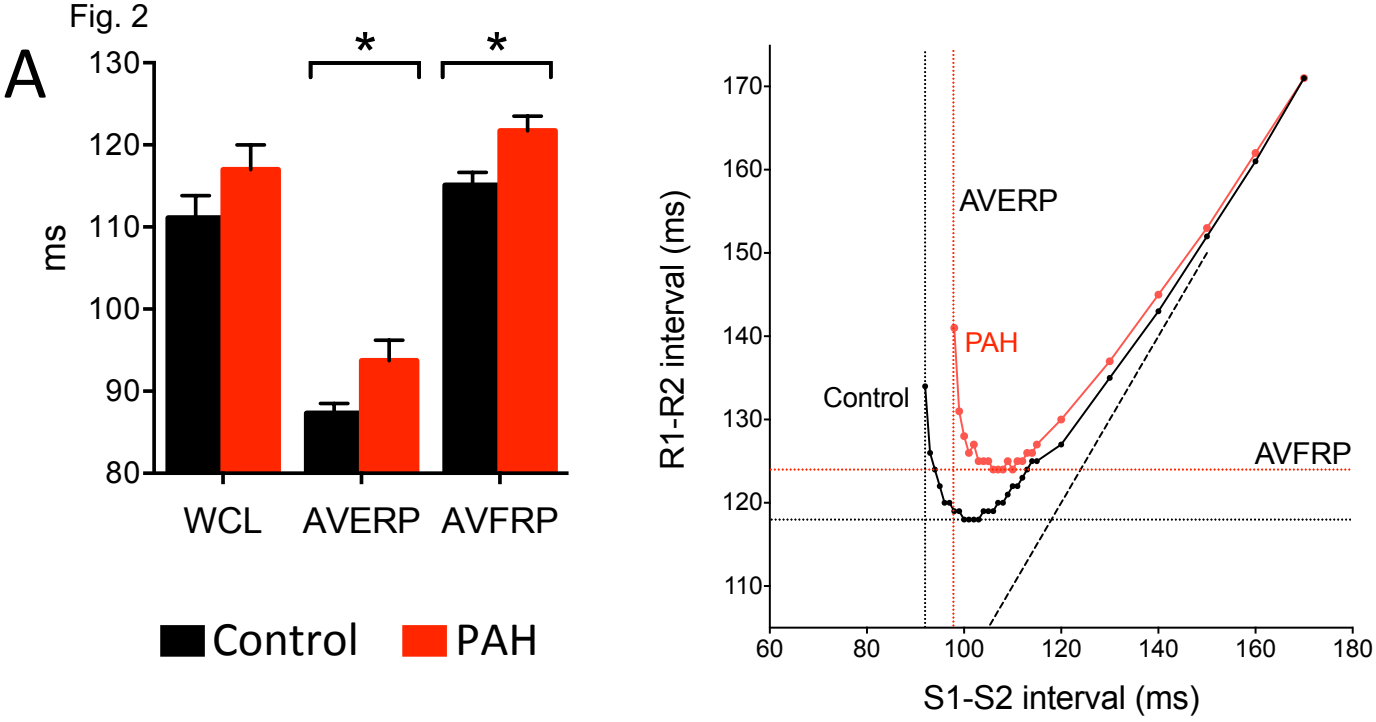
A
ms
130
120
110
100
90
80
*
*
WCL
AVERP
AVFRP
Control
PAH
R1-R2 interval (ms)
170
160
150
140
130
120
110
AVERP
PAH
Control
AVFRP
60
80
100
120
140
160
180
S1-S2 interval (ms)

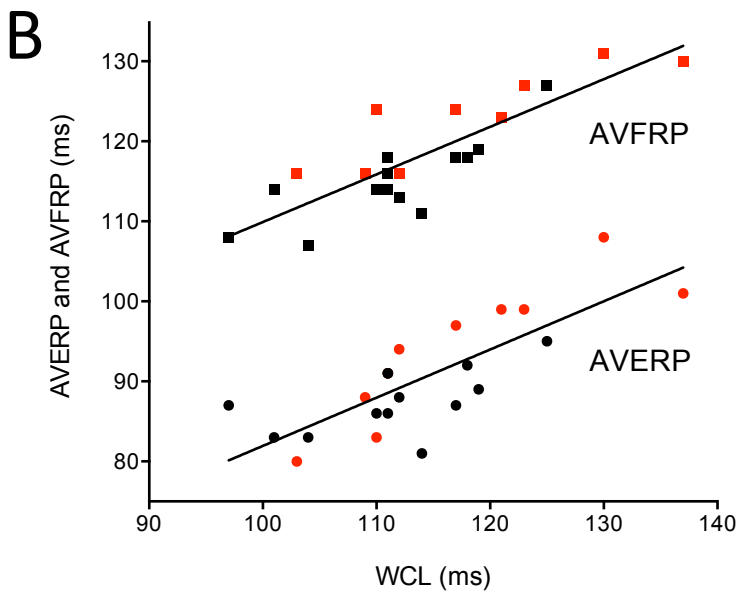
B
AVERP and AVFRP (ms)
130
120
110
100
90
80
AVFRP
AVERP
90
100
110
120
130
140
WCL (ms)

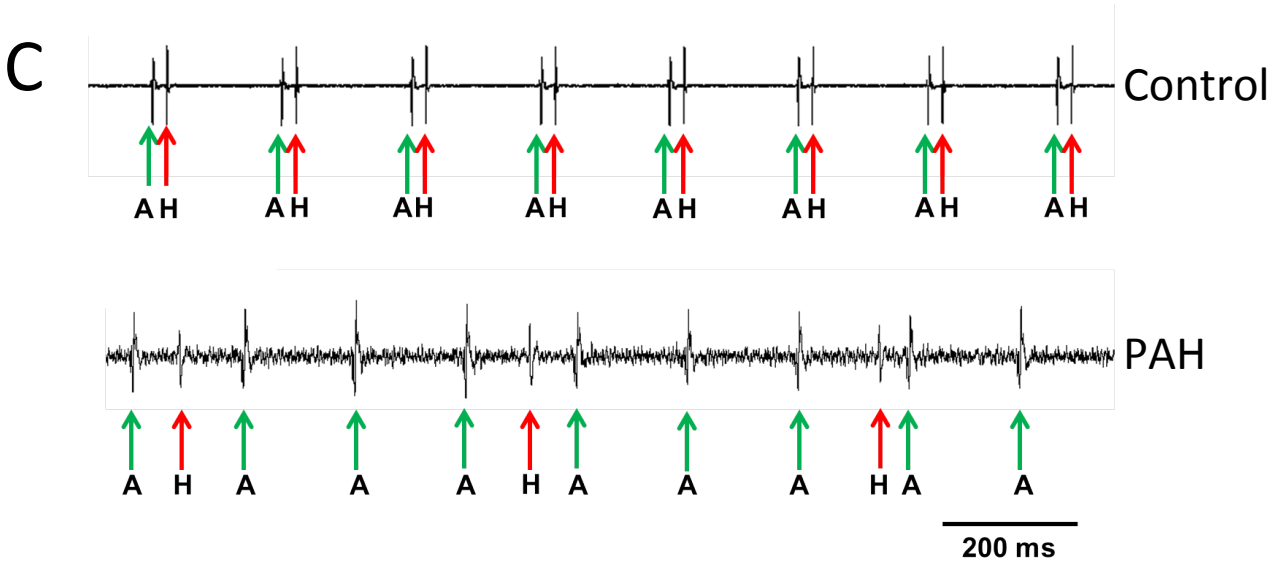
C
Control
A H
PAH
A H A A A H A A A H A
200 ms

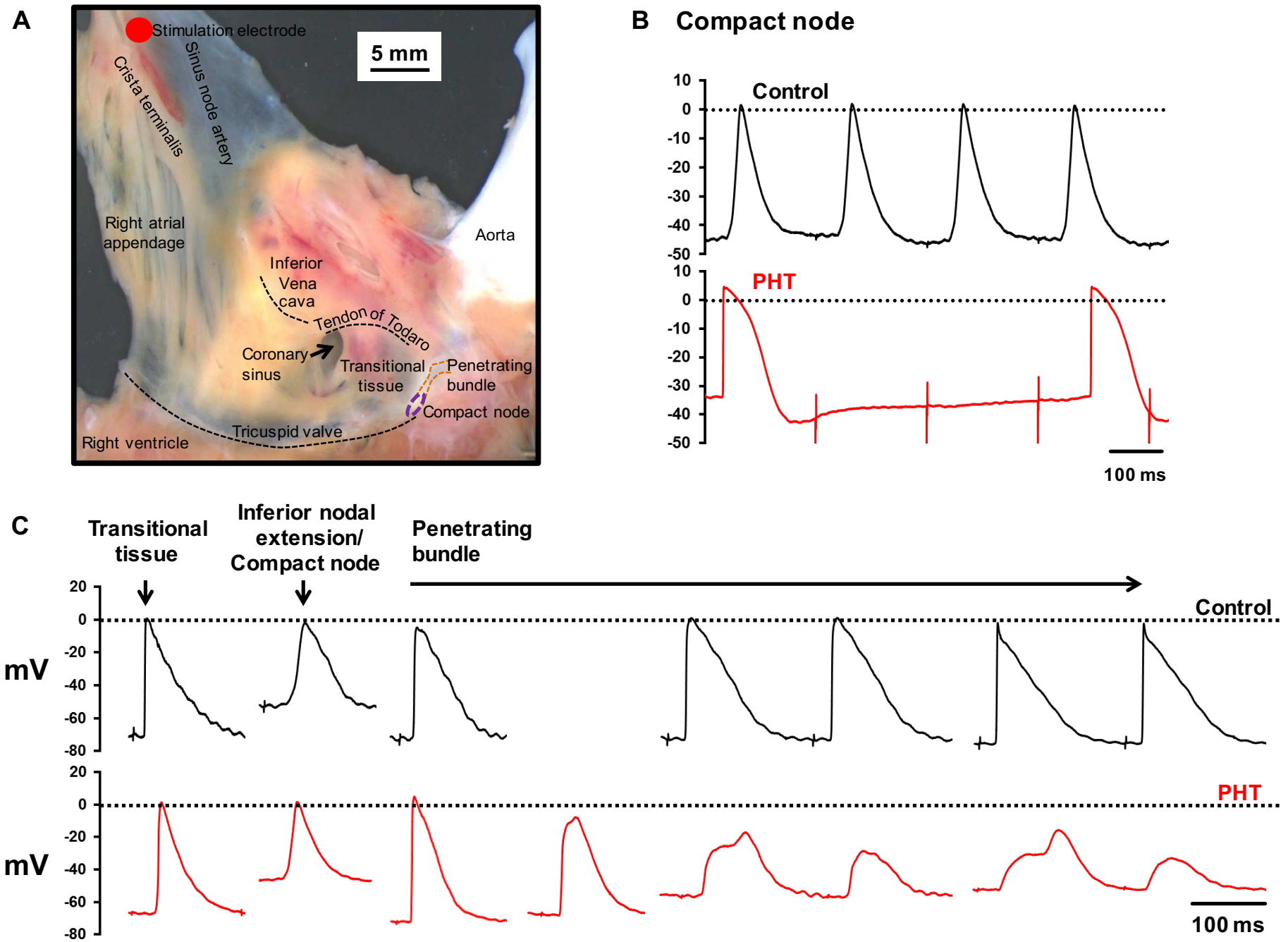
A
Stimulation electrode
5 mm
Crista terminalis
Sinus node artery
Right atrial appendage
Aorta
Inferior Vena cava
Tendon of Todaro
Coronary sinus
Transitional tissue
Penetrating bundle
Compact node
Tricuspid valve
Right ventricle
B Compact node
Control
PHT
10
0
-10
-20
-30
-40
-50
100 ms
C
Transitional tissue
Inferior nodal extension/ Compact node
Penetrating bundle
Control
PHT
mV
20
0
-20
-40
-60
-80
100 ms

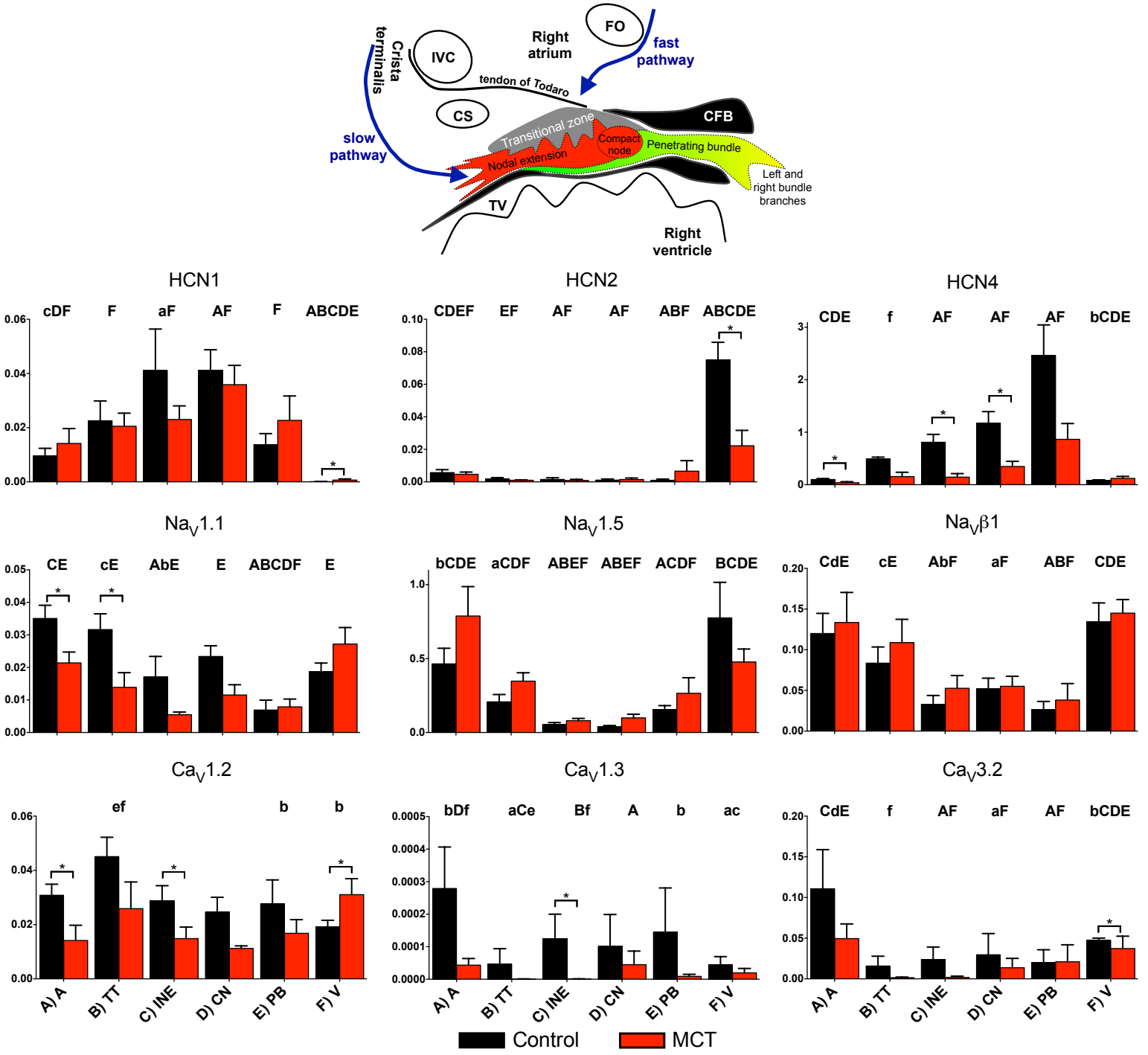
FO
Right atrium
fast pathway
Crista terminalis
IVC
tendon of Todaro
CS
CFB
Transitional zone
Compact node
Penetrating bundle
Nodal extension
slow pathway
Left and right bundle branches
TV
Right ventricle
HCN1
cDF F aF AF F ABCDE
HCN2
CDEF EF AF AF ABF ABCDE
HCN4
CDE f AF AF AF bCDE
$Na_V1.1$
CE cE AbE E ABCDF E
$Na_V1.5$
bCDE aCDF ABEF ABEF ACDF BCDE
$Na_V\beta1$
CdE cE AbF aF ABF CDE
$Ca_V1.2$
ef b b
$Ca_V1.3$
bDf aCe Bf A b ac
$Ca_V3.2$
CdE f AF aF AF bCDE
A) A
B) TT
C) INE
D) CN
E) PB
F) V
Control
MCT

Fig. 5

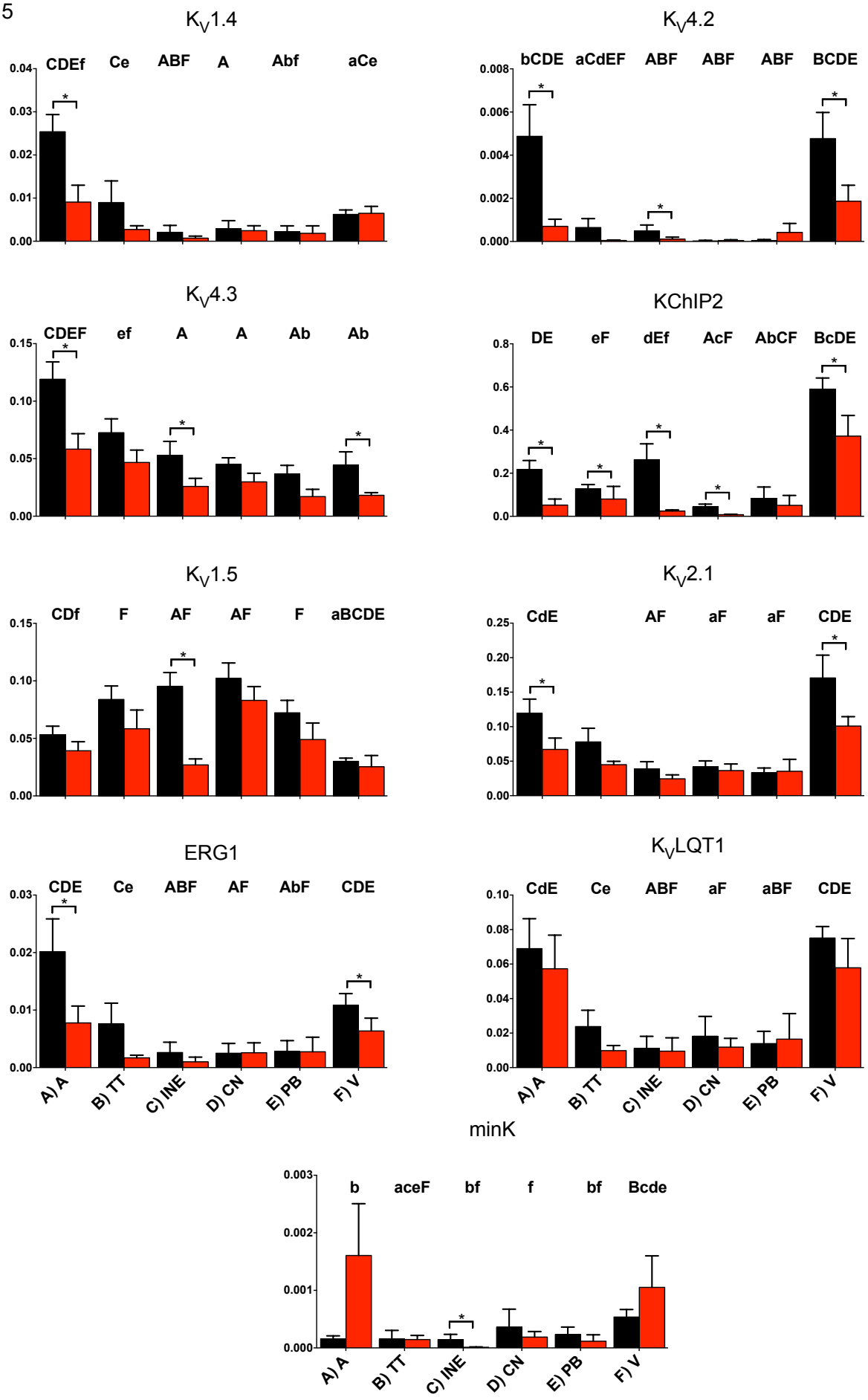
K_V1.4
CDEf Ce ABF A Abf aCe
K_V4.2
bCDE aCdEF ABF ABF ABF BCDE
K_V4.3
CDEF ef A A Ab Ab
KChIP2
DE eF dEf AcF AbCF BcDE
K_V1.5
CDf F AF AF F aBCDE
K_V2.1
CdE AF aF aF CDE
ERG1
CDE Ce ABF AF AbF CDE
K_VLQT1
CdE Ce ABF aF aBF CDE
A) A
B) TT
C) INE
D) CN
E) PB
F) V
minK
b aceF bf f bf Bcde

Fig. 6

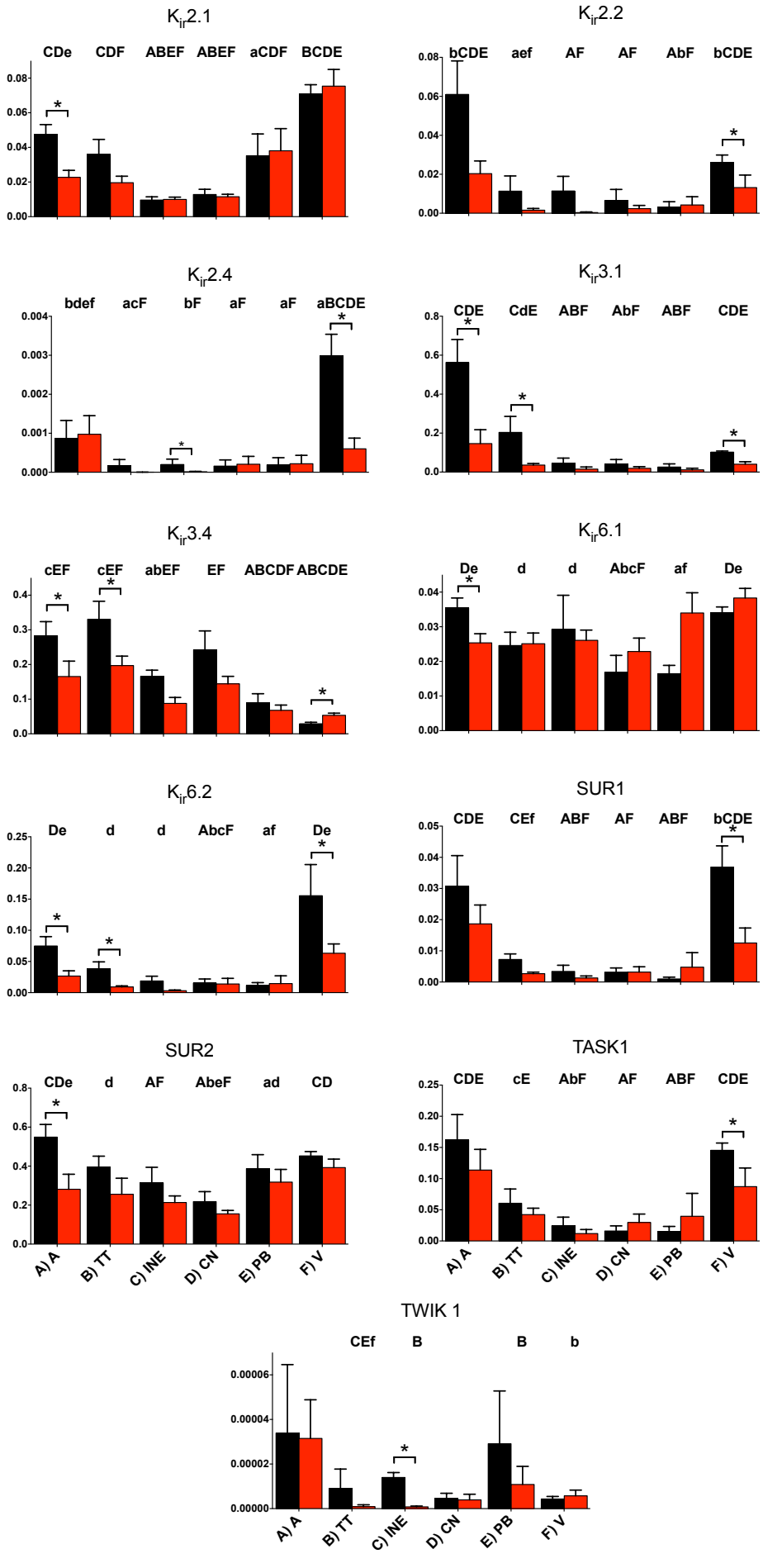
$K_{ir}2.1$
CDe CDF ABEF ABEF aCDF BCDE
$K_{ir}2.2$
bCDE aef AF AF AbF bCDE
$K_{ir}2.4$
bdef acF bF aF aF aBCDE
$K_{ir}3.1$
CDE CdE ABF AbF ABF CDE
$K_{ir}3.4$
cEF cEF abEF EF ABCDF ABCDE
$K_{ir}6.1$
De d d AbcF af De
$K_{ir}6.2$
De d d AbcF af De
SUR1
CDE CEf ABF AF ABF bCDE
SUR2
CDe d AF AbeF ad CD
TASK1
CDE cE AbF AF ABF CDE
A) A
B) TT
C) INE
D) CN
E) PB
F) V
TWIK 1
CEf B B b

Fig. 7

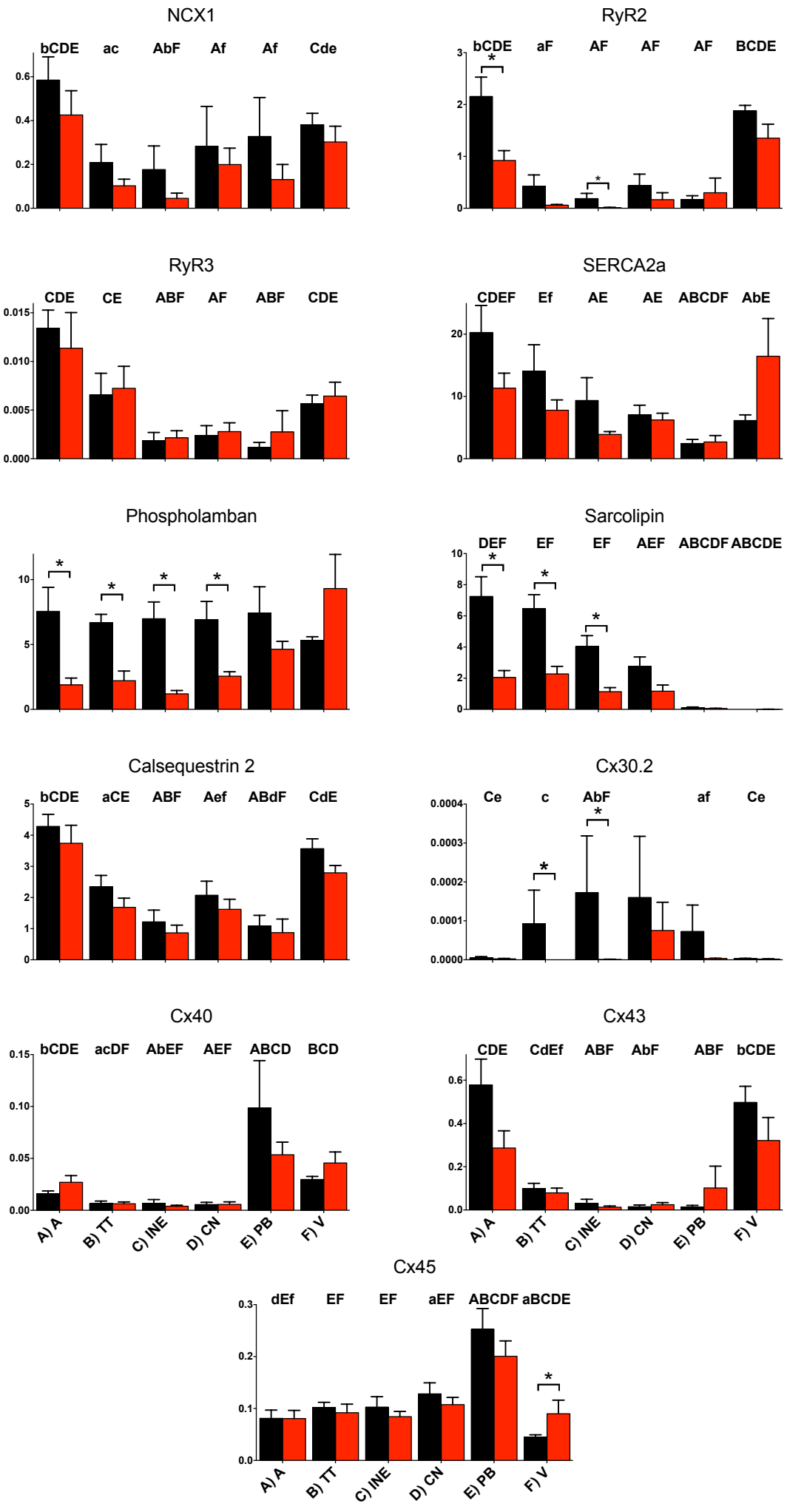
NCX1
bCDE ac AbF Af Af Cde
RyR2
bCDE aF AF AF AF BCDE
RyR3
CDE CE ABF AF ABF CDE
SERCA2a
CDEF Ef AE AE ABCDF AbE
Phospholamban
Sarcolipin
DEF EF EF AEF ABCDF ABCDE
Calsequestrin 2
bCDE aCE ABF Aef ABdF CdE
Cx30.2
Ce c AbF af Ce
Cx40
bCDE acDF AbEF AEF ABCD BCD
Cx43
CDE CdEf ABF AbF ABF bCDE
A) A
B) TT
C) INE
D) CN
E) PB
F) V
Cx45
dEf EF EF aEF ABCDF aBCDE

Fig. 8

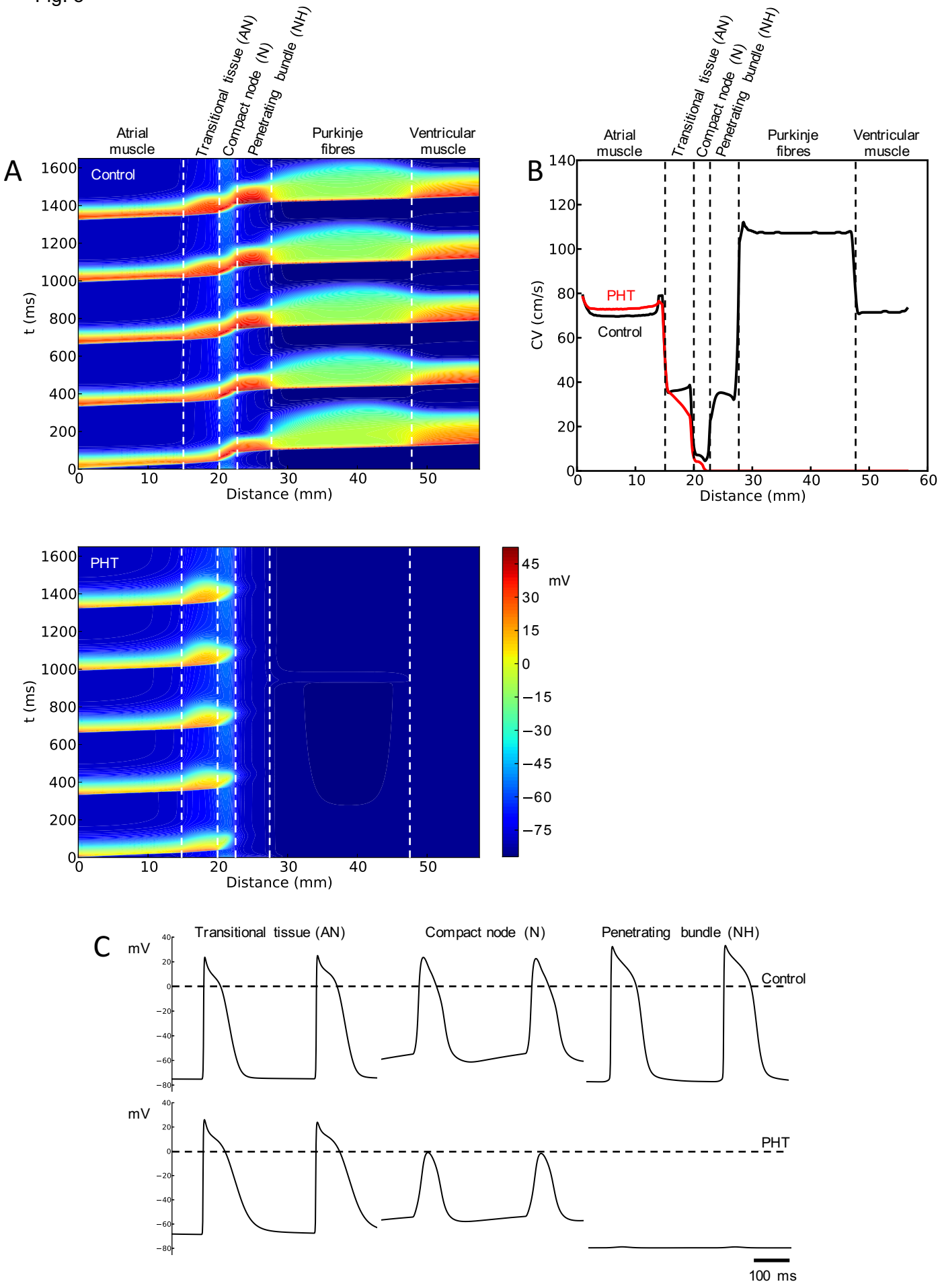
A
Atrial muscle
Transitional tissue (AN)
Compact node (N)
Penetrating bundle (NH)
Purkinje fibres
Ventricular muscle
Control
PHT
t (ms)
Distance (mm)
mV
B
CV (cm/s)
PHT
Control
C
Transitional tissue (AN)
Compact node (N)
Penetrating bundle (NH)
mV
Control
PHT
100 ms

SUPPLEMENTAL MATERIAL

Supplemental Methods

All procedures were carried out in accordance with the UK Animals Scientific Procedures Act (1986). Male Wistar rats (weight 200 g; Charles River, UK) were arbitrarily assigned to either a control or monocrotaline group. On day 0 the monocrotaline group received monocrotaline (Sigma-Aldrich Ltd, UK) 60 mg/kg by intraperitoneal injection and the control group received a volume matched 0.9% saline intraperitoneal injection (3 ml/kg). Monocrotaline was dissolved in 1 M hydrochloric acid and then made up to a concentration of 20 mg/ml with 0.9% saline, the pH corrected to 7.4 using 4 M NaOH. The animals were weighed and their clinical condition was assessed twice weekly in the first 18 days, and daily thereafter. The control and monocrotaline-injected animals were paired. Animals were sacrificed on the day that the following pre-specified endpoints were met, namely evidence of clinical deterioration with reduced movement, increased respiratory rate, piloerection and weight loss of >10 g over two days. The paired animal was sacrificed within 24 h. Animals that did not meet these criteria were electively sacrificed on day 28. The animals were sacrificed by stunning and cervical dislocation; the heart and lungs were excised and weighed.

In vivo ECG and echocardiography

Echocardiography and ECG recording was carried out under general anaesthesia with 2% isoflurane. Echocardiography images were acquired on an ACUSON Sequoia (Acuson Universal Diagnostics Solution, USA) with a 15 MHz 15L8 transducer. All images were stored on optical media disks for subsequent offline analysis. M-mode recordings were taken in the parasternal short axis view allowing recording of left ventricle anterior and posterior wall thickness and the internal diameter of the left ventricle in both systole and diastole. Right ventricle wall thickness was measured from M-mode recordings in the parasternal long axis view. Continuous wave Doppler recordings through the pulmonary artery were used to assess the pulmonary velocity profile. The maximum pulmonary velocity, time from the onset of pulmonary outflow to maximal flow (PAAT) and the rate of deceleration of pulmonary flow (PAD) were measured. ECG electrodes were inserted subcutaneously with the negative electrode in the right forepaw, the positive electrode in the left forepaw and the ground electrode in the right hindpaw. The electrodes were connected to a Bioamp and Powerlab analog to digital converter (AD Instruments, New Zealand). Signals were recorded using LabChart (AD Instruments, New Zealand) and analysed offline. Echocardiography and ECG recording was carried out on day 0 immediately prior to injection, day 21 and immediately prior to termination.

Telemetry

Telemetric recordings of ECGs from conscious and unrestrained male Wistar rats were made as part of an on-going study at the University of Leeds with UK Home Office and local ethical approval. For data included in this publication, animal source, monocrotaline treatment and experimental end points were the same as those described above with the additional voluntary ingestion of 2 ml/day blackcurrant juice placebo in the ongoing study. Implantation of recording devices and ECG acquisition were as previously described by Benoist *et al*.[1] Data were analysed using Chart 7 software (AD Instruments, New Zealand). Twenty-one days after injection of monocrotaline, ECGs were recorded 24 h per day.

Langendorff experiments

The heart was mounted on a Langendorff column and retrogradely perfused with oxygenated Tyrode's solution at a temperature of 36.5˚C with a fixed flow rate of 0.11 ml/g/min. Tyrode's solution contained: NaCl, 120 mM; $CaCl_2$, 1.2 mM; KCl, 4 mM; $MgSO_4$, 1.3 mM; NaH_2PO_4, 1.2 mM; $NaHC0_3$, 25.2 mM; glucose, 5.8 or 11 mM. The solution was equilibrated with 95%O_2 and 5% CO_2. Widely spaced extracellular electrodes were placed on the right atrium and left ventricle. The electrodes were connected via a headstage (NL100AK, Digitimer, UK) to an amplifier (NL104A, Digitimer, UK). The signal was then filtered between 50-500 Hz (NL125/6, Digitimer, UK). The amplified and filtered signal was then converted to a digital signal using a data acquisition unit (Micro 1401, Cambridge Electronic Design, UK) and recorded and analysed using Spike 2 software (Cambridge Electronic Design, UK). The electrodes record a 'pseudo-ECG' from the Langendorff-perfused heart which is equivalent to the *in vivo* ECG. The recording from 19-20 min (i.e. immediately prior to stimulation) was exported and analysed using LabChart software. This allowed an averaged ECG of the last 100 beats before stimulation to be inspected. The RR, PR and QT intervals and the QRS duration were measured. Pacing protocols were performed to measure atrial and ventricular effective refractory periods, atrioventricular (AV) node effective and functional refractory periods (AVERP and AVFRP, respectively) and Wenckebach cycle length. The pacing protocol for AVERP and AVFRP involved pacing the atrium with a drive train of 8 beats with a 180 ms coupling interval with an extra-stimulus with a progressively shortening coupling interval until failure of conduction between the atrium and ventricles was seen. The pacing protocol for Wenckebach cycle length used burst pacing of the atrium for 30 s at a fixed

cycle length with a sequentially shortening cycle length until Wenckebach conduction was seen between the atrium and the ventricle.

Isolated AV node experiments

The heart was excised from the thorax and retrogradely perfused with oxygenated Tyrode's solution chilled to 4˚C. The heart underwent dissection in a dissection chamber whilst being constantly superfused with oxygenated Tyrode's solution. The AV node preparation was placed in a perfusion bath with recirculated Tyrode's solution at a flow rate of 50 ml/min and temperature of 36.5°C. Custom made bipolar electrodes with an interelectrode spacing of 0.2 mm were used to record signals in the atrium and at the His bundle. Signals were amplified and filtered as per the Langendorff experiments. The preparation was stimulated with pacing protocols to determine AVERP, AVFRP and Wenckebach cycle length. The pacing protocol for AVERP and AVFRP involved pacing the atrium with a drive train of 15 beats with a coupling interval of 150 or 200 ms with an extra-stimulus with a progressively shortening coupling interval until failure of conduction between the atrium and ventricles was seen. The pacing protocol for determination of the Wenckebach cycle length used burst pacing of the atrium for 30 s at a fixed cycle length with a sequentially shortening cycle length until Wenckebach conduction was seen between the atrium and the His bundle.

Intracellular action potential recordings

Isolated AV node preparations were stimulated at 5 Hz at the level of the sinus node using 2 ms, 2× threshold, constant voltage rectangular pulses. Intracellular action potentials were recorded using sharp microelectrodes (20 to 40 MΩ resistances) filled with 3 M KCl as described previously by Atkinson *et al*.[2] Briefly, data acquired at 0.005 ms intervals using WinEDR V3.3.6 software (Dr J. Dempster, University of Strathclyde, Glasgow, UK) were passed through a 10 kHz low-pass Bessel filter, amplified 10 times (Axon Instruments GeneClamp 500) and digitised (Axon Instruments Digidata 1440A) for storage on a computer for later analysis.

AV node microdissection and reverse transcription quantitative polymerase chain reaction (qPCR)

Hearts were excised and the AV node dissection was carried out in the same way as for the isolated AV node experiments. The AV node was sectioned at 50 μm in a cryostat. Sections 300 μm apart were immunolabelled for HCN4 and Cx43 and stained with Masson's trichrome (Fig. S1). The immunolabelling and staining allowed six regions in and around the AV node to be identified: atrial septal myocardium, transitional tissue, inferior nodal extension, compact node, penetrating bundle and ventricular septal myocardium. A haematoxylin and eosin stain was performed on the remaining tissues and the six different regions were identified using a Nikon SMZ800 dissecting microscope (Nikon, Japan) with x63 magnification and were dissected with a sharp needle (Fig. S1). mRNA was extracted using the MirVana kit (Life Technologies, USA) and was treated with TurboDNAse (Life Technologies) to remove any residual genomic DNA. The concentration of mRNA in each sample was measured using the Qubit system (Life Technologies) and the samples were diluted so that 16 ng of total mRNA were used for reverse transcription. SuperScript VILO Mastermix (Life Technologies) with random hexamers was used to reverse transcribe the samples to cDNA. Prior to quantification, the cDNA underwent a preamplification process (Life Technologies); see below. The cDNA was quantified using the TaqMan low density array card system (TLDA; Life Technologies) using predesigned primer sequences with a hydrolysis probe detection system. Data were analysed using a combination of ExpressionSuite (Life Techonolgies) and RealTime Statminer (Integromics, S.L., USA) software. Samples that had failed to amplify for all or most targets were omitted. Where individual targets had not amplified in a sample where the majority of targets had amplified well, the undetermined values were replaced with a C_t value of 40 to represent an assumed very low abundance of the target within that sample. Expression was normalised to the abundance of a pair of housekeeper genes, B2M and PKG1, selected from 16 potential housekeeper genes as the most stable.

Preamplification

Because the tissues making up the AV node are small, the amount of RNA could be small (16 ng; less than the recommended minimum of 30 ng for Taqman low-density array cards) and therefore a preamplification step was performed after the RNA had been reverse transcribed to produce cDNA.[3,4] Preamplification of the cDNA was carried out using PCR and the combination of the specific primer sets for the genes of interest. The process of preamplification has been shown to increase the sensitivity of qPCR in several tissues,[3,4] but has not previously been used with heart tissue. To validate preamplification, 25 atrial and ventricular samples were used: 6 atrial and 7 ventricular samples from control rats and 6 atrial and 6 ventricular samples from monocrotaline-injected rats. Atrial and ventricular samples were used because relatively large amounts of RNA were isolated. From the samples, two cDNA dilutions were prepared from each: one with an effective initial total RNA of 16 ng (which was preamplified) and another with an effective initial total RNA of 160 ng (which was not preamplified). qPCR using Taqman low-density array cards was then used to

measure the expression of the 95 transcripts of interest in the samples using both dilutions. Expression was normalised to the abundance of the housekeeper genes, B2M and PKG1 (ΔC_t=C_t housekeeper–C_t target). If preamplification is effective, the ΔC_t value for a target transcript should be the same for the unamplified and preamplified samples. Fig. S2 shows the relationship between the ΔC_t values from the unamplified and preamplified samples for all transcripts and all tissue samples. The ΔC_t values for the unamplified and preamplified samples are significantly correlated ($P<0.0001$) with an R^2 value of 0.61. The correlation is excellent for abundantly expressed transcripts ($\Delta C_t<0$; transcript of interest more abundant than housekeeper). However, there is deviation from a 1:1 relationship for poorly expressed transcripts ($\Delta C_t>0$; transcript of interest less abundant than housekeeper). It is likely that low concentrations of cDNA for targets in the unamplified samples were at the limit of detection of qPCR and therefore inaccurate quantification of these targets in the unamplified samples caused deviation from the 1:1 relationship. These findings support the validity of the preamplification methodology and show the need for preamplification with the low concentrations of mRNA in the microdissected tissue samples from the AV node.

Immunohistochemistry

Whole hearts were cryosectioned, the different regions of the cardiac conduction system including the AV node identified by histology and neurofilament 150 and HCN4 immunolabelled as described previously.[5-7]

Computer modelling

mRNA is an important determinant of protein (and therefore function), although not the only determinant (it can account for ~40% of variation[8-10]). In the cardiac conduction system, we have usually (but not always) seen a correlation between mRNA and protein.[e.g.11] We and others have successfully used biophysically-detailed action potential models to predict potential changes in electrical activity based on changes in mRNA expression for ion channels etc.[11-16] We scale the conductance for a particular ionic current based on the change in the corresponding mRNA. This is not a method of generating definitive biophysically-detailed action potential models, but instead is a form of bioinformatics to explore the *possible* consequences of changes in transcripts and we have used this approach in the present study. A one-dimensional (1D) strand model of cardiac tissue was constructed in order to simulate the functional effects of pulmonary hypertension (PHT) on action potential conduction. The 1D model is 52.5 mm in length and consists of segments of atrium (15 mm), AV node (12.5 mm), Purkinje fibre (20 mm) and ventricle (10 mm). The segments were simulated by well-established models of the action potential of an atrial cell,[17] AV node cells,[18] Purkinje cell and left ventricular cell[19] of the rabbit heart (action potential models are not available for other species). Details of the dimensions and coupling conductances of the 1D strand model are summarised in Table S4. For simplicity, we chose to only consider the fast pathway (the normal pathway) through the AV node. For initiation of cardiac excitation, a series of supra-threshold stimuli were applied at the beginning of the strand of atrium; each stimulus evoked an action potential that propagated from the atrium to the AV node, and then to the Purkinje fibres and ventricular muscle. The PHT condition was simulated based on regional changes in mRNA expression, which we assumed to reflect changes in the corresponding ion channel current density as we and others have done previously.[11-16] The ratio of an ionic conductance in PHT to the same ionic conductance in control, g'_{ion}, was calculated as follows:

$$g'_{ion} = \frac{\left(\sum_{i=1}^{n} \gamma_{ion}^{i} d_{ion}^{i}\right)_{PHT}}{\left(\sum_{i=1}^{n} \gamma_{ion}^{i} d_{ion}^{i}\right)_{control}},$$

where γ_{ion} is the single channel conductance (values used listed in Table S5) and d_{ion} is the density (or expression) of the relevant ion channel. In many cases, more than one ion channel contributes to an ionic conductance and the ionic conductance was calculated by summing the contribution of the different ion channels. Details of the calculations are shown in Tables S6-S10. The changes made to simulate PHT are summarised in Table S11. The 1D cable equation was solved using the Forward-Time Central-Space scheme with a space step of 0.1 mm and time step of 0.005 ms.

Supplemental Discussion

Validation of the monocrotaline model

There are several animal models of PHT and the monocrotaline model is the best characterised and most widely used.[20,21] Monocrotaline is a pyrrolizidine alkaloid, extracted from the plant *Crotalaria spectabilis*, and a single injection has been shown to generate severe pulmonary arterial hypertension in several species, notably the rat.[e.g.22,23] Experiments using the monocrotaline model have given positive results from drug therapies including ERAs, sildenafil, statins and β-blockers that have gone on to become the mainstay of therapy for patients with pulmonary arterial hypertension.[24-28] The monocrotaline model has been used to investigate arrhythmias in the working myocardium.[1,16,29] Although the monocrotaline model is widely used

there remain some concerns over its representativeness as a model of PHT.[30] Histological examination of the lungs of monocrotaline-injected rats shows medial thickening and muscular hypertrophy, but not the characteristic plexiform lesions that are seen in patients with PHT.[30] There is also concern regarding the possibility that monocrotaline may have a direct effect on the heart and therefore any changes seen in cardiac function may be attributable to a direct effect of monocrotaline and not PHT. One study demonstrated inflammation in the right ventricular free wall, interventricular septum and posterior left ventricular wall in response to monocrotaline injection with some evidence of inflammation in the posterior left ventricle wall prior to the development of PHT. The authors argue that this demonstrates a direct toxic effect of monocrotaline on the heart.[31] In contrast to this, another study using both *in vivo* single-photon emission computed tomography imaging and *ex vivo* histological and PCR techniques demonstrated that inflammation was largely confined to the right ventricle and interventricular septum. The authors argue that inflammation is part of the pathogenesis of right heart failure secondary to PHT rather than a direct monocrotaline effect.[32] Support for this view comes from the finding of right ventricular inflammation in a rat model of pulmonary embolism and PHT.[33] The conflicting findings regarding left ventricular involvement in the monocrotaline model may in part be explained by which areas of the left ventricle were studied; the study reporting inflammation in the left ventricle looked at the posterior wall which is in close proximity to the septum and posterior attachment of the right ventricle.[31] There are several arguments that support the use of the monocrotaline model to investigate the effects of PHT. The success of several pharmacological therapies showing beneficial effects on respiratory physiology and cardiac function in both the monocrotaline model and in humans would not be expected if the deleterious effects on cardiac function seen in the monocrotaline model were purely due to a direct toxic effect of monocrotaline.[24-26,34] In our study, we are interested in the effects of PHT on the heart and therefore concerns regarding the lack of plexiform lesions in the monocrotaline model are less relevant given the known increases in right heart pressures with the monocrotaline model. The monocrotaline model is technically simple (with a single subcutaneous injection developing a severe PHT phenotype in 3-4 weeks), well characterised and has previously been used to investigate arrhythmias in the working myocardium.

Site of conduction block

The experimental data in Fig. 3 and Table S1 shows that heart block most often occurs in the compact node in PHT. However, whereas many significant changes in ion channel expression were observed in the inferior nodal extension, fewer were observed in the compact node (Table S3). However, the same trend of downregulation of L-type Ca^{2+} channels was observed in the compact node as in the inferior nodal extension (Fig. 4). The computer model, which was based on the measured changes in ion channel expression, predicted block in the compact node (Fig. 8). There is therefore a reasonable correlation between observation and prediction.

Limitations of the study

In vivo the AV node dysfunction was generally relatively modest (Table 1). As argued above, in part this is because AV node function may be supported *in vivo* by an increase in sympathetic tone. However, in addition, the animal legislation in the UK does not permit animals reaching end stage heart failure. In this study, gene expression has been measured at the mRNA level. Determination of protein expression is difficult. For example, many ion channel antibodies are poor and the specialised tissues of the heart of small mammals are too small for Western blot. However, in a pilot experiment we confirmed that there is a downregulation of HCN4 protein in the AV node in PHT (Fig. S8) consistent with the downregulation of HCN4 mRNA (Fig. 4).

Supplemental References

1. Benoist D, Stones R, Drinkhill MJ, Benson AP, Yang Z, Cassan C, Gilbert SH, Saint DA, Cazorla O, Steele DS, Bernus O and White E. Cardiac arrhythmia mechanisms in rats with heart failure induced by pulmonary hypertension. *American Journal of Physiology - Heart and Circulatory Physiology*. 2012;302:H2381-95.
2. Atkinson AJ, Logantha SJ, Hao G, Yanni J, Fedorenko O, Sinha A, Gilbert SH, Benson AP, Buckley DL, Anderson RH, Boyett MR and Dobrzynski H. Functional, anatomical, and molecular investigation of the cardiac conduction system and arrhythmogenic atrioventricular ring tissue in the rat heart. *Journal of the American Heart Association*. 2013;2:e000246.
3. Demarest TG, Murugesan N, Shrestha B and Pachter JS. Rapid expression profiling of brain microvascular endothelial cells by immuno-laser capture microdissection coupled to TaqMan low density array. *Journal of Neuroscience Methods*. 2012;206:200-4.

4. Ishii S, Segawa T and Okabe S. Simultaneous quantification of multiple food- and waterborne pathogens by use of microfluidic quantitative PCR. *Applied and Environmental Microbiology*. 2013;79:2891-8.
5. Yanni J, Boyett MR, Anderson RH and Dobrzynski H. The extent of the specialized atrioventricular ring tissues. *Heart Rhythm*. 2009;6:672-680.
6. Yanni J, Tellez JO, Sutyagin PV, Boyett MR and Dobrzynski H. Structural remodelling of the sinoatrial node in obese old rats. *Journal of Molecular and Cellular Cardiology*. 2010;48:653-662.
7. Dobrzynski H, Li J, Tellez J, Greener ID, Nikolski VP, Wright SE, Parson SH, Jones SA, Lancaster MK, Yamamoto M, Honjo H, Takagishi Y, Kodama I, Efimov IR, Billeter R and Boyett MR. Computer three-dimensional reconstruction of the sinoatrial node. *Circulation*. 2005;111:846-854.
8. Tian Q, Stepaniants SB, Mao M, Weng L, Feetham MC, Doyle MJ, Yi EC, Dai H, Thorsson V, Eng J, Goodlett D, Berger JP, Gunter B, Linseley PS, Stoughton RB, Aebersold R, Collins SJ, Hanlon WA and Hood LE. Integrated genomic and proteomic analyses of gene expression in Mammalian cells. *Molecular & Cellular Proteomics*. 2004;3:960-9.
9. Fu N, Drinnenberg I, Kelso J, Wu JR, Paabo S, Zeng R and Khaitovich P. Comparison of protein and mRNA expression evolution in humans and chimpanzees. *PLoS One*. 2007;2:e216.
10. Maier T, Guell M and Serrano L. Correlation of mRNA and protein in complex biological samples. *FEBS Letters*. 2009;583:3966-73.
11. Chandler NJ, Greener ID, Tellez JO, Inada S, Musa H, Molenaar P, DiFrancesco D, Baruscotti M, Longhi R, Anderson RH, Billeter R, Sharma V, Sigg DC, Boyett MR and Dobrzynski H. Molecular architecture of the human sinus node - insights into the function of the cardiac pacemaker. *Circulation*. 2009;119:1562-1575.
12. Abd Allah ESH, Tellez JO, Aslanidi OV, Zhang H, Dobrzynski H and Boyett MR. Postnatal development of transmural gradients in expression of ion channels and Ca^{2+}-handling proteins in the ventricle. *Journal of Molecular and Cellular Cardiology*. 2012;53:145-155.
13. Dobrzynski H, Anderson RH, Atkinson A, Borbas Z, D'Souza A, Fraser JF, Inada S, Logantha SJRJ, Monfredi O, Morris GM, Moorman AFM, Nikolaidou T, Schneider H, Szuts V, Temple IP, Yanni J and Boyett MR. Structure, function and clinical relevance of the cardiac conduction system, including the atrioventricular ring and outflow tract tissues. *Pharmacology & Therapeutics*. 2013;139:260-288.
14. Hao XZ, Y.; Zhang, X.; Nirmalan, M.; Davies, L.; Dobrzynski, H.; Wang, X.; Grace, A.A.; Zhang, H., Boyett, M.R.; Huang, C.L.-H.; Lei, M. TGF-β1 mediated fibrosis and ion channel remodeling are key mechanisms producing sinus node dysfunction associated with SCN5A deficiency and aging. *Circulation: Arrhythmia and Electrophysiology*. 2011;4:397-406.
15. Li J, Logantha SJ, Yanni J, Cai X, Dobrzynski H, Hart G and Boyett M. Computer simulation of failing rabbit Purkinje fibres. *Computers in Cardiology*. 2013;40:361-364.
16. Benoist D, Stones R, Drinkhill M, Bernus O and White E. Arrhythmogenic substrate in hearts of rats with monocrotaline-induced pulmonary hypertension and right ventricular hypertrophy. *American Journal of Physiology*. 2011;300:H2230-H2237.
17. Aslanidi OV, Dewey RS, Morgan AR, Boyett MR and Zhang H. Regional differences in rabbit atrial action potential properties: mechanisms, consequences and pharmacological implications. *Conference Proceedings of IEEE Engineering in Medicine & Biology Society*. 2008;2008:141-144.
18. Inada S, Hancox JC, Zhang H and Boyett MR. One-dimensional mathematical model of the atrioventricular node including atrio-nodal, nodal, and nodal-his cells. *Biophysical Journal*. 2009;97:2117-2127.
19. Aslanidi OV, Sleiman RN, Boyett MR, Hancox JC and Zhang H. Ionic mechanisms for electrical heterogeneity between rabbit Purkinje fiber and ventricular cells. *Biophysical Journal*. 2010;98:2420-31.
20. Stenmark KR, Meyrick B, Galie N, Mooi WJ and McMurtry IF. Animal models of pulmonary arterial hypertension: the hope for etiological discovery and pharmacological cure. *American Journal of Physiology*. 2009;297:L1013-32.
21. Pak O, Janssen W, Ghofrani HA, Seeger W, Grimminger F, Schermuly RT and Weissmann N. Animal models of pulmonary hypertension: role in translational research. *Drug Discovery Today: Disease Models*. 2011;7:89-97.

22. Wilson DW, Segall HJ, Pan LC and Dunston SK. Progressive inflammatory and structural changes in the pulmonary vasculature of monocrotaline-treated rats. *Microvascular Research*. 1989;38:57-80.
23. Kay JM, Harris P and Heath D. Pulmonary hypertension produced in rats by ingestion of Crotalaria spectabilis seeds. *Thorax*. 1967;22:176-9.
24. Clozel M, Hess P, Rey M, Iglarz M, Binkert C and Qiu C. Bosentan, sildenafil, and their combination in the monocrotaline model of pulmonary hypertension in rats. *Experimental Biology and Medicine*. 2006;231:967-973.
25. Hamidi SA, Lin RZ, Szema AM, Lyubsky S, Jiang YP and Said SI. VIP and endothelin receptor antagonist: an effective combination against experimental pulmonary arterial hypertension. *Respiratory Research*. 2011;12:141.
26. Iglarz M, Binkert C, Morrison K, Fischli W, Gatfield J, Treiber A, Weller T, Bolli MH, Boss C, Buchmann S, Capeleto B, Hess P, Qiu C and Clozel M. Pharmacology of macitentan, an orally active tissue-targeting dual endothelin receptor antagonist. *Journal of Pharmacology and Experimental Therapeutics*. 2008;327:736-45.
27. McMurtry MS, Bonnet S, Michelakis ED, Bonnet S, Haromy A and Archer SL. Statin therapy, alone or with rapamycin, does not reverse monocrotaline pulmonary arterial hypertension: the rapamcyin-atorvastatin-simvastatin study. *American Journal of Physiology - Lung Cellular and Molecular Physiology*. 2007;293:L933-40.
28. Mouchaers KT, Schalij I, Versteilen AM, Hadi AM, van Nieuw Amerongen GP, van Hinsbergh VW, Postmus PE, van der Laarse WJ and Vonk-Noordegraaf A. Endothelin receptor blockade combined with phosphodiesterase-5 inhibition increases right ventricular mitochondrial capacity in pulmonary arterial hypertension. *American Journal of Physiology - Heart and Circulatory Physiology*. 2009;297:H200-7.
29. Uzzaman M, Honjo H, Takagishi Y, Emdad L, Magee AI, Severs NJ and Kodama I. Remodeling of gap junctional coupling in hypertrophied right ventricles of rats with monocrotaline-induced pulmonary hypertension. *Circulation Research*. 2000;86:871-878.
30. Stenmark KR, Meyrick B, Galie N, Mooi WJ and McMurtry IF. Animal models of pulmonary arterial hypertension: the hope for etiological discovery and pharmacological cure. *American Journal of Physiology - Lung Cellular and Molecular Physiology*. 2009;297:L1013-32.
31. Akhavein F, St-Michel EJ, Seifert E and Rohlicek CV. Decreased left ventricular function, myocarditis, and coronary arteriolar medial thickening following monocrotaline administration in adult rats. *Journal of Applied Physiology*. 2007;103:287-95.
32. Campian ME, Hardziyenka M, de Bruin K, van Eck-Smit BL, de Bakker JM, Verberne HJ and Tan HL. Early inflammatory response during the development of right ventricular heart failure in a rat model. *European Journal of Heart Failure*. 2010;12:653-8.
33. Watts JA, Zagorski J, Gellar MA, Stevinson BG and Kline JA. Cardiac inflammation contributes to right ventricular dysfunction following experimental pulmonary embolism in rats. *Journal of Molecular and Cellular Cardiology*. 2006;41:296-307.
34. Dupuis J and Prie S. The ET(A)-receptor antagonist LU 135252 prevents the progression of established pulmonary hypertension induced by monocrotaline in rats. *Journal of cardiovascular pharmacology and therapeutics*. 1999;4:33-39.
35. Brandt MC, Endres-Becker J, Zagidullin N, Motloch LJ, Er F, Rottlaender D, Michels G, Herzig S and Hoppe UC. Effects of KCNE2 on HCN isoforms: distinct modulation of membrane expression and single channel properties. *American Journal of Physiology - Heart and Circulatory Physiology*. 2009;297:H355-63.
36. Vanoye CG, Lossin C, Rhodes TH and George AL, Jr. Single-channel properties of human $Na_v1.1$ and mechanism of channel dysfunction in SCN1A-associated epilepsy. *Journal of General Physiology*. 2006;127:1-14.
37. Beyder A, Rae JL, Bernard C, Strege PR, Sachs F and Farrugia G. Mechanosensitivity of Nav1.5, a voltage-sensitive sodium channel. *Journal of Physiology*. 588:4969-85.
38. Navedo MF, Amberg GC, Westenbroek RE, Sinnegger-Brauns MJ, Catterall WA, Striessnig J and Santana LF. $Ca_v1.3$ channels produce persistent calcium sparklets, but $Ca_v1.2$ channels are responsible for sparklets in mouse arterial smooth muscle. *American Journal of Physiology - Heart and Circulatory Physiology*. 2007;293:H1359-70.
39. Bittner KC and Hanck DA. The relationship between single-channel and whole-cell conductance in the T-type Ca^{2+} channel $Ca_v3.1$. *Biophysical Journal*. 2008;95:931-41.

40. Zhu J, Watanabe I, Gomez B and Thornhill WB. Heteromeric Kv1 potassium channel expression: amino acid determinants involved in processing and trafficking to the cell surface. *Journal of Biological Chemistry*. 2003;278:25558-67.
41. Wang Z, Eldstrom JR, Jantzi J, Moore ED and Fedida D. Increased focal Kv4.2 channel expression at the plasma membrane is the result of actin depolymerization. *American Journal of Physiology - Heart and Circulatory Physiology*. 2004;286:H749-59.
42. Jerng HH, Qian Y and Pfaffinger PJ. Modulation of Kv4.2 channel expression and gating by dipeptidyl peptidase 10 (DPP10). *Biophysical Journal*. 2004;87:2380-96.
43. Liu GX, Derst C, Schlichthorl G, Heinen S, Seebohm G, Bruggemann A, Kummer W, Veh RW, Daut J and Preisig-Muller R. Comparison of cloned Kir2 channels with native inward rectifier K^+ channels from guinea-pig cardiomyocytes. *Journal of Physiology*. 2001;532:115-126.
44. Boyett MR, Inada S, Yoo S, Li J, Liu J, Tellez JO, Greener ID, Honjo H, Billeter R, Lei M, Zhang H, Efimov IR and Dobrzynski H. Connexins in the sinoatrial and atrioventricular nodes. *Advances in Cardiology*. 2006;42:175-197.

Table S1. Normal and abnormal electrical conduction through the isolated AV node from control and PHT rats.

Conduction phenotype	Incidence	
	Control	PHT
Normal 1:1 conduction through AV node	4/5	1/6
Conduction block in compact node (e.g. Fig. 3B)	1/5	3/6
Decremental conduction in penetrating bundle and likely complete block (Fig. 3C)	0/5	1/6
Decremental conduction in the penetrating bundle	0/5	1/6

Table S2. Expression of all transcripts. Expression of a transcript is given as a percentage of the expression of the same transcript in the control atrial sample. Significant differences (FDR<0.2) between the control and PHT groups are marked with arrows. A red highlighted arrow indicates significant downregulation in the PHT group and a green highlighted arrow indicates significant upregulation in the PHT group. MCT, monocrotaline.

	Atrium		Transitional tissue		Inferior nodal extension		Compact node		Penetrating bundle		Ventricle	
	Control	MCT	Control	MCT	Control	MCT	Control	MCT	Control	MCT	Control	MCT
Inward currents												
$Na_V1.1$	100	61 ↓	90	40 ↓	49	16	67	33	20	23	53	78
$Na_V1.5$	100	169	45	75	11	17	9	21	33	57	167	103
$Na_V1.8$	100	47	16	18	9	88	4	40	687	347	3	7 ↑
$Na_V\beta1$	100	111	70	91	27	44	43	46	22	32	112	121
$Ca_V1.2$	100	46 ↓	146	84	93	48 ↓	80	36	90	54	62	101 ↑
$Ca_V1.3$	100	16	17	0	45	0 ↓	36	16	52	3	16	7
$Ca_V3.1$	100	38	41	8	39	9	45	46	30	5	14	10
$Ca_V3.2$	100	45	14	1	22	2	27	12	18	19	43	34 ↓
$Ca_V\alpha2\delta1$	100	77	21	15	18	5	9	8	7	15	71	45
$Ca_V2\delta2$	100	83	18	3	31	4	48	79	111	9	58	30 ↓
$Ca_V\beta2$	100	113	42	34	15	18	23	36	17	29	87	128
HCN1	100	147	234	213	426	239	426	372	143	235	1	7 ↑
HCN2	100	80	32	17	27	16	20	25	18	114	1299	385 ↓
HCN4	100	39 ↓	487	154	800	143 ↓	1162	343 ↓	2428	853	78	119
CLC-2	100	71	98	77	58	30	69	69	69	91	86	82
CLC-3	100	79	87	72	182	71 ↓	117	106	133	143	55	156 ↑

Table S2 (continued).

	Atrium		Transitional tissue		Inferior nodal extension		Compact node		Penetrating bundle		Ventricle	
	Control	**MCT**	**Control**	**MCT**	**Control**	**MCT**	**Control**	**MCT**	**Control**	**MCT**	**Control**	**MCT**
Outward currents												
Kv1.2	100	9 ↓	17	1	9	0 ↓	3	2	15	2	20	7
Kv1.4	100	36 ↓	35	11	8	3	12	10	9	7	25	26
Kv1.5	100	74	158	109	179	51 ↓	192	156	136	92	57	48
Kv2.1	100	56 ↓	65	38	33	20	35	30	28	30	143	84 ↓
Kv4.2	100	14 ↓	13	1	10	2 ↓	1	1	1	9	97	38 ↓
Kv4.3	100	49 ↓	61	39	45	22 ↓	38	25	31	14	37	15 ↓
ERG1	100	39 ↓	38	8	13	5	13	13	14	14	54	32 ↓
K_VLQT1	100	83	35	14	16	14	26	17	20	24	109	84
K_{ir}2.1	100	48 ↓	76	41	20	21	27	24	74	80	149	159
K_{ir}2.2	100	33	19	3	19	1	11	4	5	7	43	22 ↓
K_{ir}2.4	100	117	20	0	24	2 ↓	24	2	23	26	357	72 ↓
K_{ir}3.1	100	26 ↓	36	6 ↓	8	3	7	3	5	2	18	7 ↓
K_{ir}3.4	100	58 ↓	117	70	59	31 ↓	86	51	32	24	10	19 ↑
K_{ir}6.1	100	72 ↓	69	71	83	74	48	65	46	96	96	108
K_{ir}6.2	100	36 ↓	51	12 ↓	25	4	21	19	16	19	208	84 ↓
SUR1	100	60	24	9	11	4	10	10	3	15	120	41 ↓
SUR2	100	51 ↓	72	47	57	39	40	28	71	58	82	72
KChIP2	100	24 ↓	59	37 ↓	121	11 ↓	21	4 ↓	39	23	270	170 ↓
minK	100	1060	104	96	98	8 ↓	240	124	154	77	354	694
TWIK1	100	93	27	3	41	2 ↓	13	12	86	32	14	17
TASK1	100	70	37	26	15	7	10	18	9	24	90	54 ↓

Table S2 (continued).

	Atrium		Transitional tissue		Inferior nodal extension		Compact node		Penetrating bundle		Ventricle	
	Control	**MCT**	**Control**	**MCT**	**Control**	**MCT**	**Control**	**MCT**	**Control**	**MCT**	**Control**	**MCT**
Intracellular Ca^{2+} cycling												
RyR2	100	43 ↓	20	3	9	1 ↓	20	8	8	14	87	63
RyR3	100	85	49	54	14	16	18	21	9	21	42	48
NCX1	100	73	36	18	30	8	48	34	56	22	65	52
SERCA2a	100	56	69	38	46	19	35	31	12	13	30	81
Phospholamban	100	25 ↓	88	29 ↓	93	18 ↓	92	34 ↓	98	61	70	123
PMCA1	100	103	71	69	84	58	77	68	80	82	91	69
Calsequestrin 2	100	87	55	39	29	20	48	38	25	20	83	65
Sarcolipin	100	28 ↓	89	31 ↓	56	16 ↓	38	16	2	1	0	0
Connexins												
Cx30.2	100	47	1743	1 ↓	3249	20 ↓	3012	1415	1374	65	55	35
Cx43	100	50	17	14	5	2	3	4	2	18	86	56
Cx40	100	170	41	40	43	25	35	36	622	337	188	287
Cx45	100	99	125	113	127	104	158	132	311	247	55	111↑
Ion channel transporters												
Na^+/K^+ ATPase α1 subunit	100	71	114	94	66	60	107	85	82	93	34	51↑
Na^+/K^+ ATPase α2 subunit	100	40 ↓	90	56	103	37 ↓	81	54	113	82	174	102 ↓
Na^+/K^+ ATPase α3 subunit	100	129	184	99	896	97 ↓	1078	283 ↓	405	97	210	34 ↓
Na^+/K^+ ATPase β1 subunit	100	146	30	56	16	25	22	41	21	18	68	44 ↓
Na^+/H^+ transporter	100	88	76	72	45	69 ↑	104	81	78	65	53	54

Table S2 (continued).

	Atrium		Transitional tissue		Inferior nodal extension		Compact node		Penetrating bundle		Ventricle	
	Control	**MCT**	**Control**	**MCT**	**Control**	**MCT**	**Control**	**MCT**	**Control**	**MCT**	**Control**	**MCT**
Autonomic regulators												
α1a/1c adrenergic receptor,	100	58 ↓	34	22	29	8 ↓	33	27	27	48	121	119
α1b adrenergic receptor,	100	34	23	0	24	0	22	14	17	52	370	144 ↓
β1 adrenergic receptor	100	62	103	82	88	46 ↓	85	77	68	42	80	61
β2 adrenergic receptor	100	58 ↓	121	81	99	75	95	93	63	95	81	85
M2 muscarinic receptor	100	48 ↓	23	12	14	4	13	18	5	9	25	30
A1 adenosine receptor	100	116	21	20	36	12	16	59	8	15	40	34

Table S3. Summary of transcripts significantly (FDR<0.2) altered in the different regions of the AV node in PHT. Red downward arrow, downregulation in PHT; green upward arrow, upregulation. *P* value from limma test and FDR-corrected *P* value given.

Atrial muscle	P value	Adjusted P value	Transitional tissue	P value	Adjusted P value	Inferior nodal extension	P value	Adjusted P value
HCN4 ↓	<0.01	0.03	$Na_v1.1$ ↓	0.01	0.10	HCN4 ↓	<0.01	<0.01
$Na_v1.1$ ↓	0.05	0.17	KChIP2 ↓	0.02	0.14	$Ca_v1.2$ ↓	0.06	0.18
$Ca_v1.2$ ↓	0.01	0.04	$K_{ir}3.1$ ↓	0.01	0.10	$Ca_v1.3$ ↓	<0.01	<0.01
$K_v1.4$ ↓	<0.01	0.04	$K_{ir}6.2$ ↓	<0.01	0.06	CLC-3 ↓	0.06	0.18
$K_v4.2$ ↓	0.02	0.07	Phospholamban ↓	<0.01	0.03	$K_v4.2$ ↓	0.06	0.19
$K_v4.3$ ↓	0.01	0.04	Sarcolipin ↓	<0.01	0.04	$K_v4.3$ ↓	0.05	0.18
KChIP2 ↓	<0.01	0.02	Cx30.2 ↓	0.01	0.10	KChIP2 ↓	<0.01	<0.01
$K_v1.2$ ↓	<0.01	0.04				$K_v1.2$ ↓	0.04	0.17
$K_v2.1$ ↓	0.05	0.17				$K_v1.5$ ↓	<0.01	<0.01
ERG1 ↓	0.06	0.17				minK ↓	0.02	0.10
$K_{ir}2.1$ ↓	0.01	0.04				$K_{ir}2.4$ ↓	0.01	0.04
$K_{ir}3.1$ ↓	0.01	0.04				$K_{ir}3.4$ ↓	0.01	0.08
$K_{ir}3.4$ ↓	0.04	0.14				TWIK1 ↓	<0.01	<0.01
$K_{ir}6.1$ ↓	0.06	0.19				RyR2 ↓	<0.01	0.02
$K_{ir}6.2$ ↓	0.01	0.04				Phospholamban ↓	<0.01	<0.01
SUR2 ↓	0.01	0.04				Sarcolipin ↓	<0.01	0.02
RyR2 ↓	0.02	0.07				Cx30.2 ↓	<0.01	<0.01
Phospholamban ↓	<0.01	0.01				Na^+/K^+ ATPase α2 subunit ↓	<0.01	0.02
Sarcolipin ↓	<0.01	0.01				Na^+/K^+ ATPase α3 subunit ↓	<0.01	<0.01
Na^+/K^+ ATPase α2 subunit ↓	<0.01	0.03				Na^+/H^+ transporter ↑	0.07	0.20
M2 muscarinic receptor ↓	0.05	0.17				1a/1c adrenergic receptor ↓	0.02	0.09
1a/1c adrenergic receptor ↓	0.03	0.11				β1 adrenergic receptor ↓	0.06	0.18
β2 adrenergic receptor ↓	0.01	0.05						

Table S3 (continued).

Compact node	P value	Adjusted P value	Ventricular muscle	P value	Adjusted P value
HCN4 ↓	<0.01	0.03	HCN1 ↑	0.02	0.16
KChIP2 ↓	<0.01	0.03	HCN2 ↓	0.01	0.04
Phospholamban ↓	0.01	0.08	$Na_v1.8$ ↑	0.02	0.08
Na^+/K^+ ATPase α3 subunit ↓	0.01	0.08	$Ca_v1.2$ ↑	0.08	0.20
			$Ca_v3.2$ ↓	0.07	0.17
			$Ca_vα2δ2$ ↓	0.02	0.08
			CLC-3 ↑	<0.01	0.02
			$K_v4.2$ ↓	0.06	0.16
			$K_v4.3$ ↓	0.01	0.06
			KChIP2 ↓	0.02	0.08
			$K_v2.1$ ↓	0.05	0.15
			ERG1 ↓	0.07	0.18
			$K_{ir}2.2$ ↓	0.08	0.19
			$K_{ir}2.4$ ↓	<0.01	0.04
			$K_{ir}3.1$ ↓	<0.01	0.02
			$K_{ir}3.4$ ↓	0.02	0.08
			$K_{ir}6.2$ ↓	0.01	0.07
			SUR1 ↓	0.01	0.04
			TASK1 ↓	0.03	0.10
			Cx45 ↑	0.06	0.17
			Na^+/K^+ ATPase α1 subunit ↑	0.03	0.10
			Na^+/K^+ ATPase α2 subunit ↓	0.01	0.07
			Na^+/K^+ ATPase α3 subunit ↓	<0.01	0.01
			Na^+/K^+ ATPase β1 subunit ↓	0.04	0.11
			α1b adrenergic receptor ↓	0.01	0.05

Table S4. Summary of cell models used in 1D strand, strand dimensions and intercellular conductances.

Cell model	Number of cells	Length (mm)	Conductance (nS)
Atrium[17]	150	15.0	1000
Atrio-nodal[18]	50	5.0	500
Nodal[18]	25	2.5	290
Nodal-His[18]	50	5.0	500
Purkinje fibre[19]	200	20.0	3000
Left ventricle[19]	100	10.0	1150

Table S5. Single channel conductances used in calculations.

Channel	Single channel conductance
I_f	
HCN1	13.3 pS[35]
HCN4	16.9 pS[35]
I_{Na}	
$Na_v1.1$	17.0 pS[36]
$Na_v1.5$	17.3 pS[37]
$I_{Ca,L}$	
$Ca_v1.2$	19.0 pS[38]
$Ca_v1.3$	21.0 pS[38]
$I_{Ca,T}$	
$Ca_V3.1$	9.5 pS[39]
$Ca_V3.2$	7.2 pS[39]
I_{to}	
$K_v1.4$	4.0 pS[40]
$K_v4.2$	18.3 pS[41]
$K_v4.3$	4.0 pS[42]
$I_{K,1}$	
$K_{ir}2.1$	23.8 pS[43]
$K_{ir}2.2$	34.0 pS[43]
Electrical coupling	
Cx30.2	9.0 pS[44]
Cx40	200.0 pS[44]
Cx43	80.0 pS[44]
Cx45	30.0 pS[44]

Table S6. Calculation of ionic conductances in PHT in atrial muscle.

Atrium					
Current	**Protein**	**Control ($\times 10^{-4}$)**	**Pulmonary hypertension (×10-4)**	γ_{ion} (pS)	**Scaling factor for conductance (percentage)**
I_{Na}	$Na_V1.1$	351	214	17.0	162
	$Na_V1.5$	4650	7881	17.3	
$I_{Ca,L}$	$Ca_V1.2$	309	141	19.0	46
	$Ca_V1.3$	3	0	21.0	
I_{to}	$K_v1.4$	254	91	4.0	36
	$K_v4.2$	49	7	18.3	
	$K_v4.3$	1192	583	4.0	
$I_{K,ur}$ or I_{sus} or $I_{K,p}$	$K_v1.5$	533	393	-	74
$I_{K,r}$	ERG1	201	78	-	39
$I_{K,s}$	K_VLQT1	691	573	-	83
$I_{K,1}$	$K_{ir}2.1$	475	227	23.8	38
	$K_{ir}2.2$	611	203	34.0	
I_{NaCa}	NCX1	5853	4257	-	73
$I_{Ca,p}$	PMCA1	488	504	-	103
I_{NaK} or I_p	α1 Na^+-K^+ pump	16412	11570	-	68
	α2 Na^+-K^+ pump	1912	758	-	
	α3 Na^+-K^+ pump	99	128	-	
Electrical coupling	Cx30.2	0	0	9.0	59
	Cx40	159	269	200.0	
	Cx43	5780	2866	80.0	
	Cx45	812	806	30.0	

Table S7. Calculation of ionic conductances in PHT in transitional tissue.

Transitional tissue (AN cell)					
Current	**Protein**	**Control (×10^{-4})**	**Pulmonary hypertension (×10-4)**	γ_{ion} (pS)	**Scaling factor for conductance (percentage)**
I_{Na}	$Na_V1.1$	317	139	17.0	151
	$Na_V1.5$	2087	3475	17.3	
$I_{Ca,L}$	$Ca_V1.2$	451	259	19.0	57
	$Ca_V1.3$	0	0	21.0	
$I_{to,slow}$	$K_v1.4$	90	27	-	30
$I_{to,fast}$	$K_v4.2$	7	0	18.3	62
	$K_v4.3$	728	468	4.0	
$I_{K,r}$	ERG1	76	17	-	22
$I_{K,1}$	$K_{ir}2.1$	359	196	23.8	42
	$K_{ir}2.2$	114	16	34.0	
J_{rel}	RyR2	4239	596	-	16
	RyR3	66	72	-	
J_{up}	SERCA2a	140658	77857	-	55
I_{NaCa}	NCX1	2094	1026	-	49
I_{NaK} or I_p	α1 Na^+-K^+ pump	18654	15430	-	81
	α2 Na^+-K^+ pump	1729	1064	-	
	α3 Na^+-K^+ pump	182	98	-	
Electrical coupling	Cx30.2	1	0	9.0	65
	Cx40	987	791	200.0	
	Cx43	6653	3830	80.0	
	Cx45	1017	920	30.0	

Table S8. Calculation of ionic conductances in PHT in the compact node.

Compact node (N cell)					
Current	**Protein**	**Control (×10^{-4})**	**Pulmonary hypertension (×10-4)**	γ_{ion} (pS)	**Scaling factor for conductance (percentage)**
I_f	HCN1	411	359	13.3	31
	HCN2	12	15	35	
	HCN4	11775	3474	16.9	
$I_{Ca,L}$	$Ca_V1.2$	246	112	19.0	46
	$Ca_V1.3$	1	0	21.0	
$I_{to,slow}$	$K_v1.4$	29	25	-	84
$I_{to,fast}$	$K_v4.2$	0	0	18.3	67
	$K_v4.3$	451	299	4.0	
$I_{K,r}$	ERG1	25	26	-	102
J_{rel}	RyR2	4403	1670	-	38
	RyR3	24	28	-	
J_{up}	SERCA2a	70401	62299	-	88
I_{NaCa}	NCX1	2836	1996	-	70
I_{NaK} or I_p	α1 Na^+-K^+ pump	17540	13922	-	76
	α2 Na^+-K^+ pump	1546	1031	-	
	α3 Na^+-K^+ pump	1069	281	-	
Electrical coupling	Cx30.2	2	1	9.0	102
	Cx40	56	57	200.0	
	Cx43	154	247	80.0	
	Cx45	1284	1076	30.0	

Table S9. Calculation of ionic conductances in PHT in the penetrating bundle.

Penetrating Bundle (NH cell)					
Current	**Protein**	**Control (×10^{-4})**	**Pulmonary hypertension (×10-4)**	γ_{ion} (pS)	**Scaling factor for conductance (percentage)**
I_{Na}	$Na_V1.1$	70	79	17.0	169
	$Na_V1.5$	1546	2656	17.3	
$I_{Ca,L}$	$Ca_V1.2$	278	168	19.0	60
	$Ca_V1.3$	1	0	21.0	
$I_{to,slow}$	$K_v1.4$	22	18	-	84
$I_{to,fast}$	$K_v4.2$	0	4	18.3	51
	$K_v4.3$	369	170	4.0	
$I_{K,r}$	ERG1	29	28	-	96
$I_{K,1}$	$K_{ir}2.1$	352	380	23.8	111
	$K_{ir}2.2$	32	42	34.0	
J_{rel}	RyR2	1678	3005	-	180
	RyR3	12	28	-	
J_{up}	SERCA2a	24420	26945	-	110
I_{NaCa}	NCX1	3283	1313	-	40
I_{NaK} or I_p	α1 Na^+-K^+ pump	13448	15316	-	106
	α2 Na^+-K^+ pump	2169	1559	-	
	α3 Na^+-K^+ pump	402	97	-	
Electrical coupling	Cx30.2	1	0	9.0	88
	Cx40	988	535	200.0	
	Cx43	139	1022	80.0	
	Cx45	2530	2006	30.0	

Table S10. Calculation of ionic conductances in PHT in ventricular muscle.

Current	Protein	Control ($\times 10^{-4}$)	Pulmonary hypertension (×10-4)	γ_{ion} (pS)	Scaling factor for conductance (percentage)
I_{Na}	$Na_V1.1$	187	272	17.0	63
	$Na_V1.5$	7765	4776	17.3	
$I_{Ca,L}$	$Ca_V1.2$	193	310	19.0	161
	$Ca_V1.3$	0	0	21.0	
$I_{Ca,T}$	$Ca_V3.1$	78	57	9.5	77
	$Ca_v3.2$	476	373	7.2	
$I_{to,slow}$	$K_v1.4$	63	65	-	103
$I_{to,fast}$	$K_v4.2$	47	19	18.3	40
	$K_v4.3$	444	182	4.0	
$I_{K,ur}$ or I_{sus} or $I_{K,p}$	$K_v1.5$	301	254	-	84
$I_{K,r}$	ERG1	109	64	-	59
$I_{K,s}$	K_VLQT1	753	579	-	77
$I_{K,1}$	$K_{ir}2.1$	708	753	23.8	87
	$K_{ir}2.2$	262	132	34.0	
J_{rel}	RyR2	18797	13525	-	72
	RyR3	56	64	-	
J_{up}	SERCA2a	61344	164649		268
I_{NaCa}	NCX1	3811	3025	-	79
$I_{Ca,p}$	PMCA1	444	338	-	76
I_{NaK} or I_p	α1 Na^+-K^+ pump	5604	8289	-	112
	α2 Na^+-K^+ pump	3326	1942	-	
	α3 Na^+-K^+ pump	208	34	-	
Electrical coupling	Cx30.2	0	0	9.0	80
	Cx40	298	456	200.0	
	Cx43	4978	3214	80.0	
	Cx45	449	900	30.0	

Table S11. Summary of remodelling of ionic currents in PHT in different cell types. I_f, funny current; I_{Na}, Na^+ current; $I_{Ca,L}$, L-type Ca^{2+} current; $I_{Ca,T}$, T-type Ca^{2+} current; I_{to}, transient outward K^+ current; $I_{to,slow}$, slow component of I_{to}; $I_{to,fast}$, fast component of I_{to}; $I_{K,ur}$ (or I_{sus} or $I_{K,p}$), ultra-rapid delayed rectifier K^+ current; $I_{K,r}$, rapid delayed rectifier K^+ current; $I_{K,s}$, slow delayed rectifier K^+ current; $I_{K,1}$, background inward rectifier K^+ current; J_{rel}, sarcoplasmic reticulum Ca^{2+} release; J_{up}, sarcoplasmic reticulum Ca^{2+} uptake; I_{NaCa}, Na^+-Ca^{2+} exchange current; $I_{Ca,p}$ (or I_{SLCap}), sarcolemmal Ca^{2+} pump current; I_{NaK} (or I_p), Na^+-K^+ pump current.

Current	Atrial muscle	Atrio-nodal (AN) cells	Nodal (N) cells	Nodal-His (NH) cells	Purkinje fibres & ventricle
I_f	-	-	31%	-	-
I_{Na}	162%	151%	-	169%	63%
$I_{Ca,L}$	46%	57%	46%	60%	161%
$I_{Ca,T}$	-	-	-	-	77%
I_{to}	36%	-	-	-	-
$I_{to,slow}$	-	30%	84%	84%	103%
$I_{to,fast}$	-	62%	67%	51%	40%
$I_{K,ur}$ or I_{sus} or $I_{K,p}$	74%	-	-	-	84%
$I_{K,r}$	39%	22%	102%	96%	59%
$I_{K,s}$	83%	-	-	-	77%
$I_{K,1}$	38%	42%	-	111%	87%
J_{rel}	-	16%	38%	180%	72%
J_{up}	-	55%	88%	110%	268%
I_{NaCa}	73%	49%	70%	40%	79%
$I_{Ca,p}$ or I_{SLCap}	103%	-	-	-	76%
I_{NaK} or I_p	68%	81%	76%	106%	112%
Electrical coupling	59%	65%	102%	88%	80

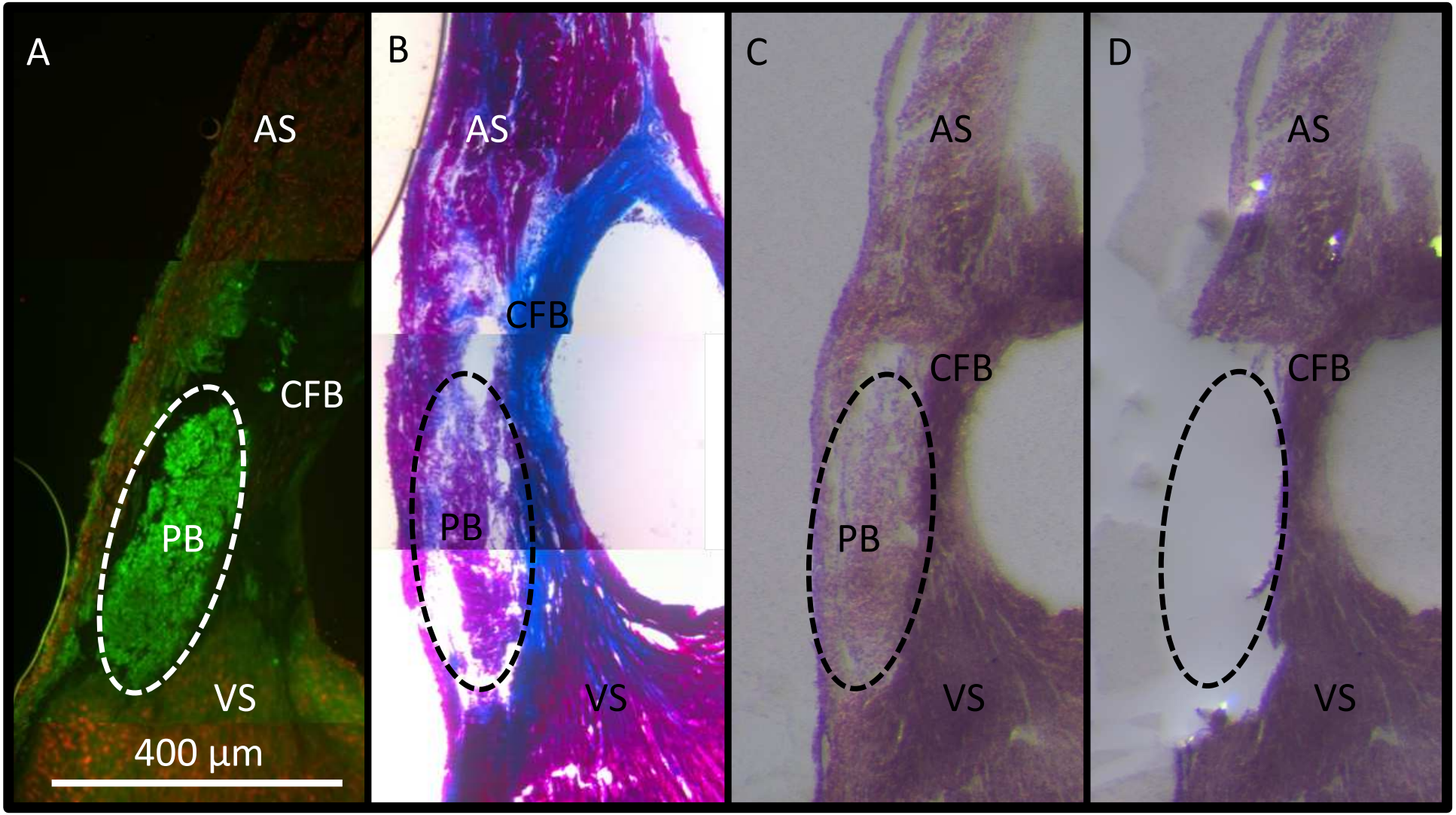

Fig. S1. Images demonstrating hand microdissection of the AV node. A, AV node section double immunolabelled for HCN4 (green) and Cx43 (red). The ringed area shows high levels of HCN4 and low levels of Cx43 and corresponds to the penetrating bundle (PB). B, Masson's trichrome staining of a 'sister section'. The area of interest demonstrated in panel A can be seen to be bordered by the central fibrous body (stained bright blue). The combination of high levels of HCN4, low levels of Cx43 and the presence of the central fibrous body identifies this area as the penetrating bundle (PB). C, haematoxylin and eosin stained section before microdissection. This reveals the area of interest identified from the 'map' created by the images in panels A and B. D, the same slide as C post-microdissection with the area of interest (in this case the penetrating bundle) removed. AS, atrial septum; CFB, central fibrous body; VS, ventricular septum.

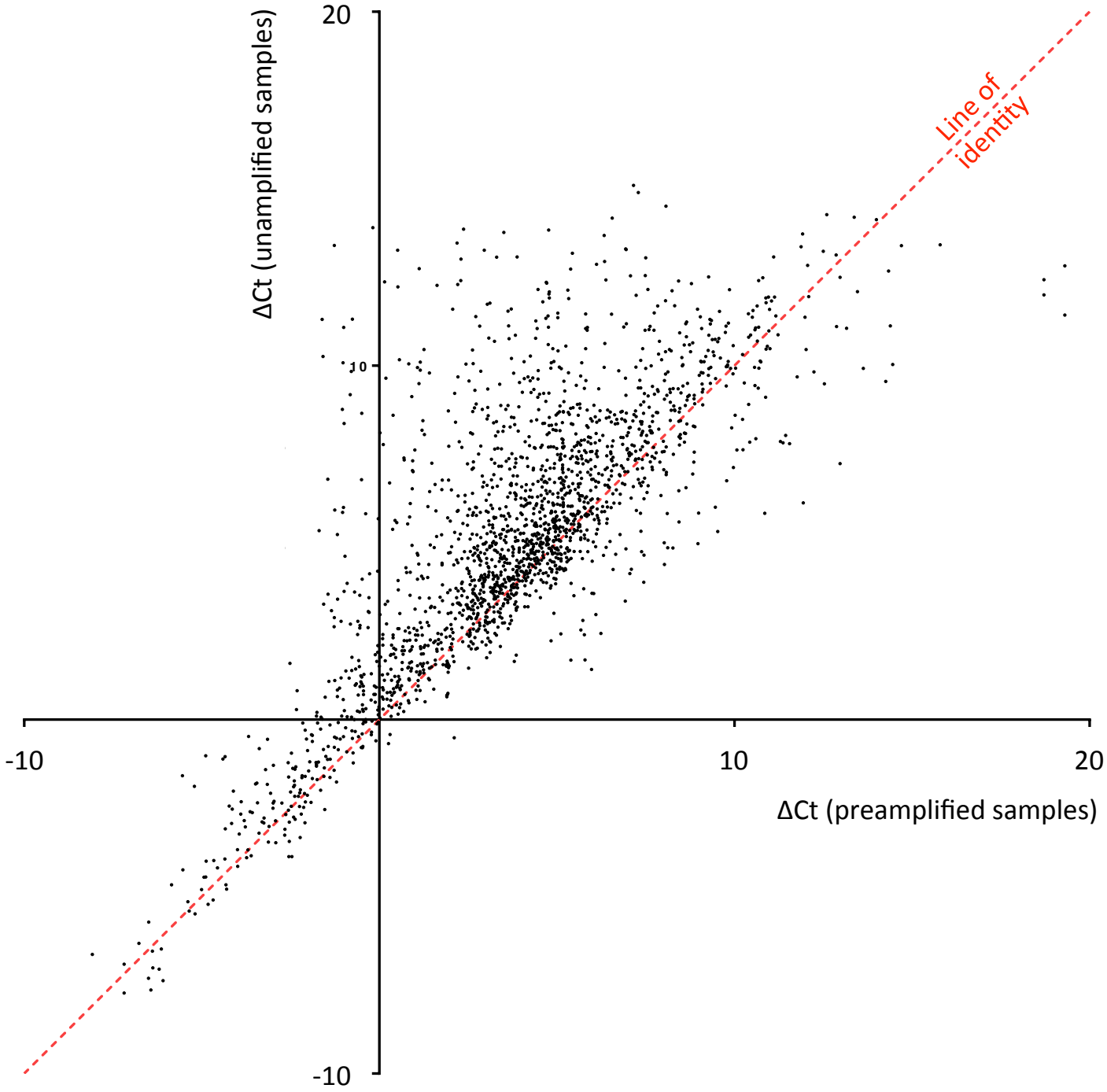

Fig. S2. Correlation of mRNA abundance (relative to that of the housekeeper; ΔCT) in unamplified and preamplified samples from the atrium and ventricle. See text for details. Linear regression analysis showed a significant correlation between the two ($R^2 = 0.62$; $P<0001$).

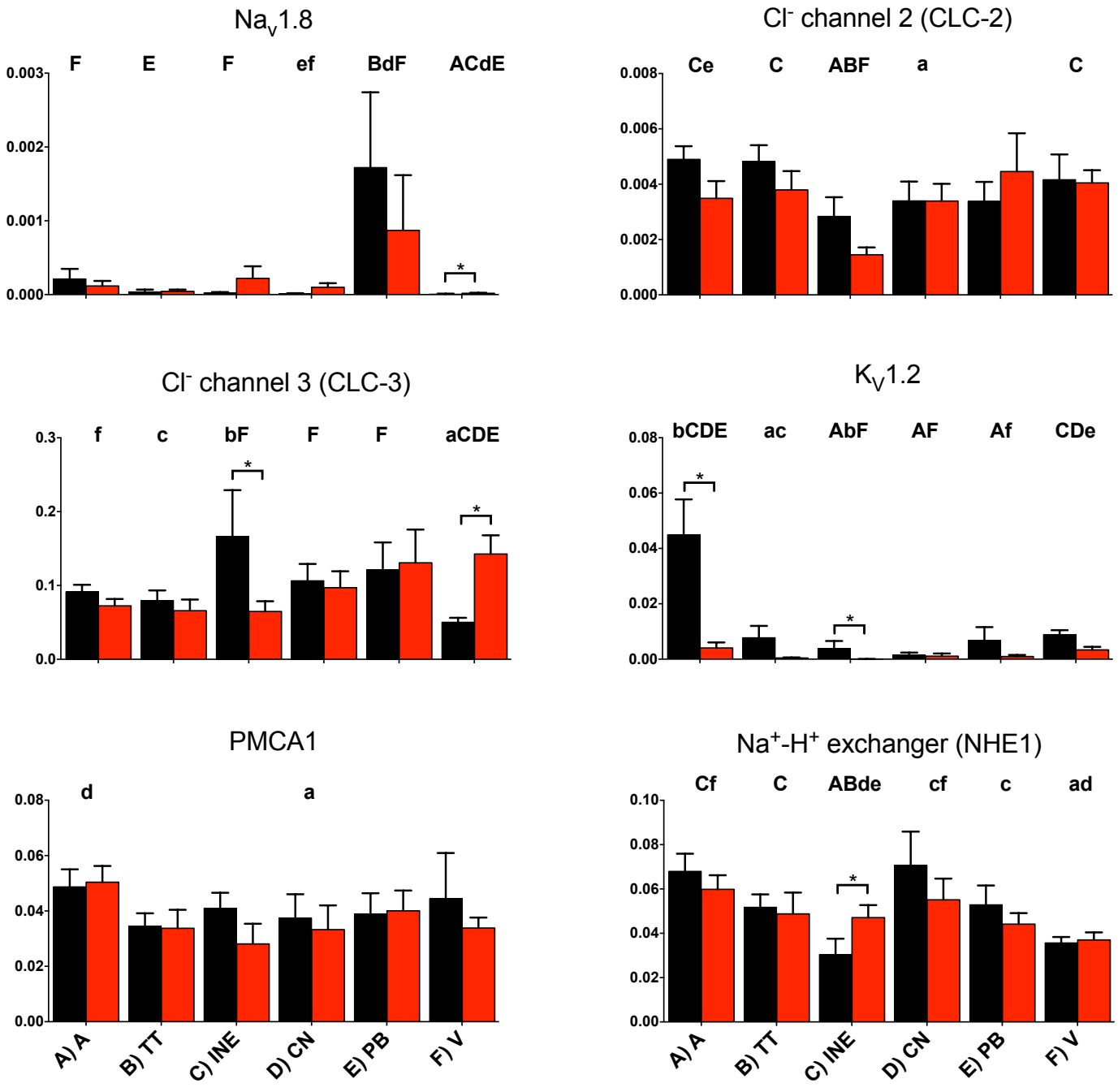

Fig. S3. Expression of miscellaneous transcripts in atrial muscle (A; A), transitional tissue (B; TT), inferior nodal extension (C; INE), compact node (D; CN), penetrating bundle (E; PB) and ventricular muscle (F; V) from control (black bars) and PHT (PHT; red bars) rats. In this and similar figures, means (+SEM) shown (n=6-8) and bars and asterisks indicate significant differences between the control and PHT rats assessed by the limma test (FDR-corrected $P<0.2$, i.e. 20%); for the control tissues only, letters indicate a significant difference from the appropriately lettered region (lower case letters, FDR-corrected $P<0.2$, i.e. 20%; upper case letters, FDR-corrected $P<0.05$, i.e. 5%).

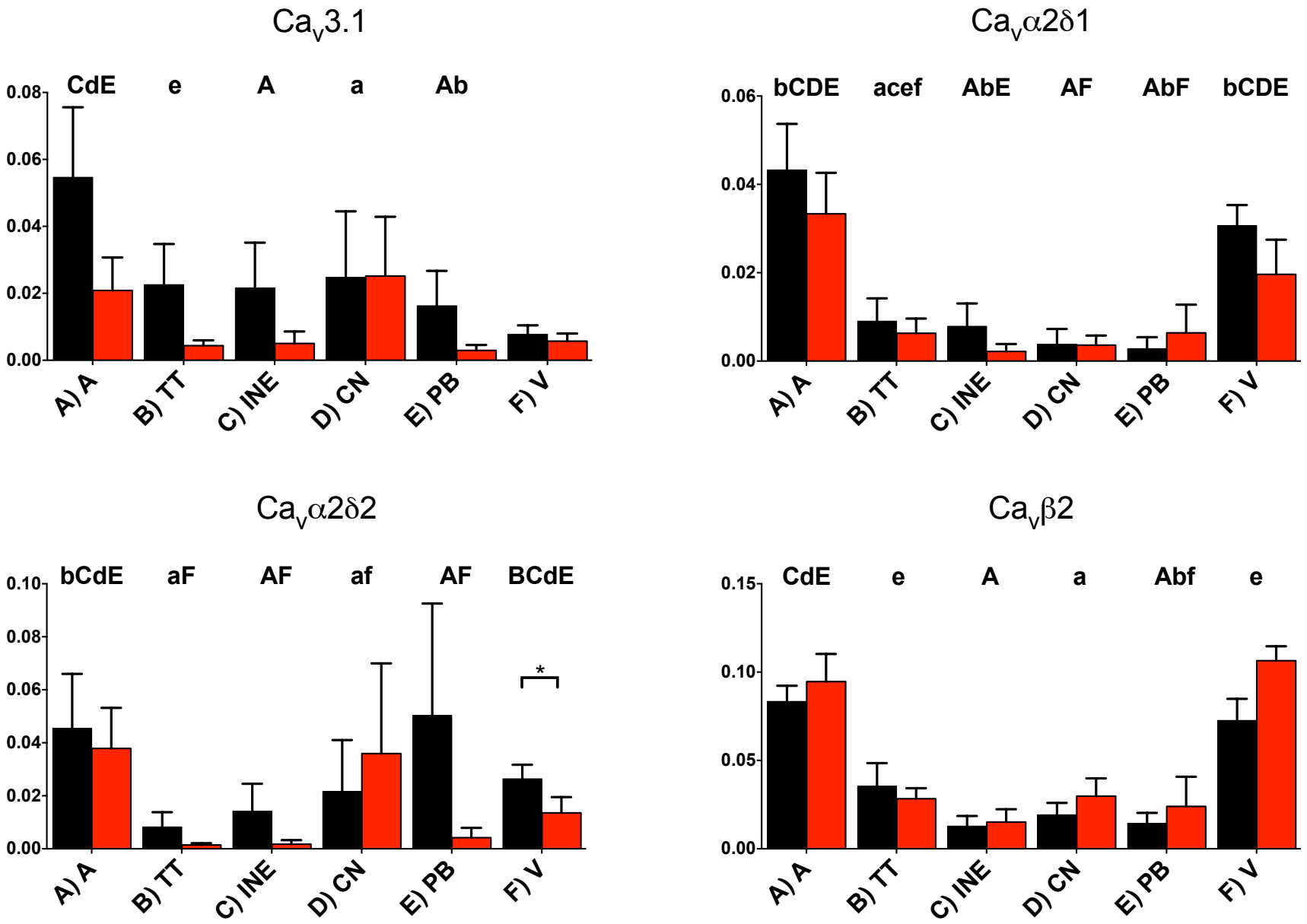

Fig. S4. Expression at the mRNA level of Ca^{2+} channel subunits in atrial muscle (A; A), transitional tissue (B; TT), inferior nodal extension (C; INE), compact node (D; CN), penetrating bundle (E; PB) and ventricular muscle (F; V) from control (black bars) and PHT (red bars) rats.

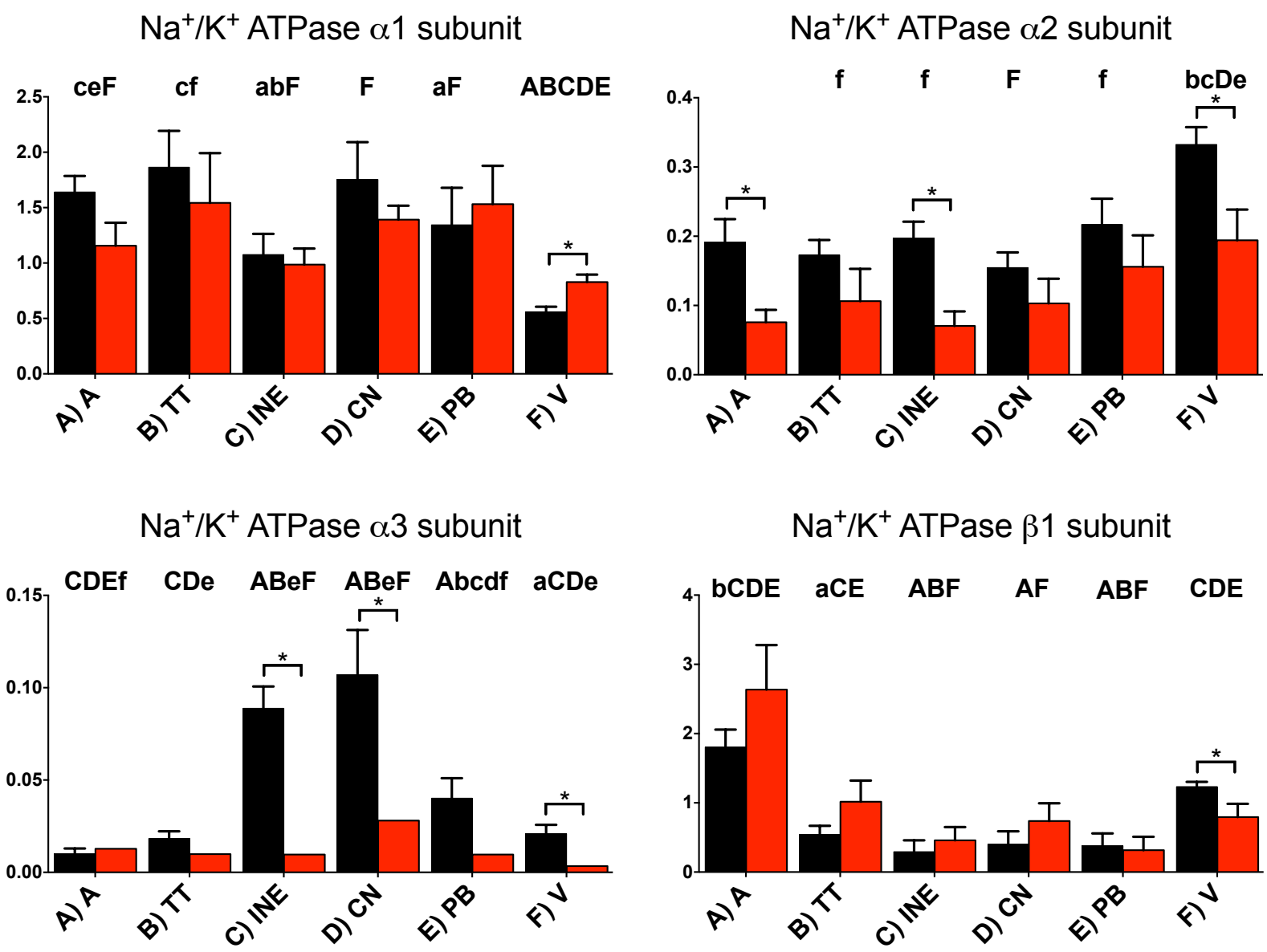

Fig. S5. Expression at the mRNA level of Na^+-K^+ pump subunits in atrial muscle (A; A), transitional tissue (B; TT), inferior nodal extension (C; INE), compact node (D; CN), penetrating bundle (E; PB) and ventricular muscle (F; V) from control (black bars) and PHT (red bars) rats.

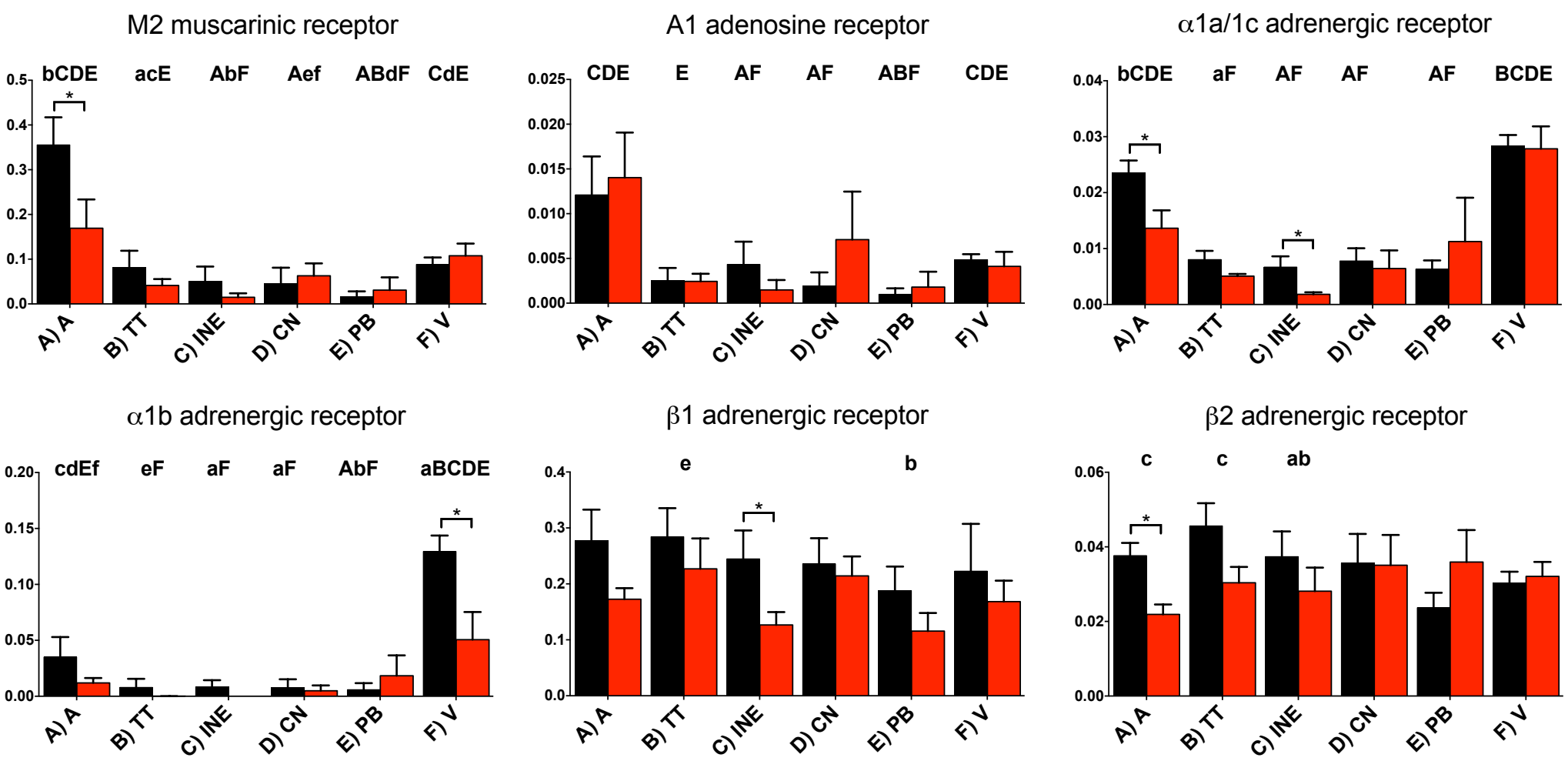

Fig. S6. Expression at the mRNA level of receptors in atrial muscle (A; A), transitional tissue (B; TT), inferior nodal extension (C; INE), compact node (D; CN), penetrating bundle (E; PB) and ventricular muscle (F; V) from control (black bars) and PHT (red bars) rats.

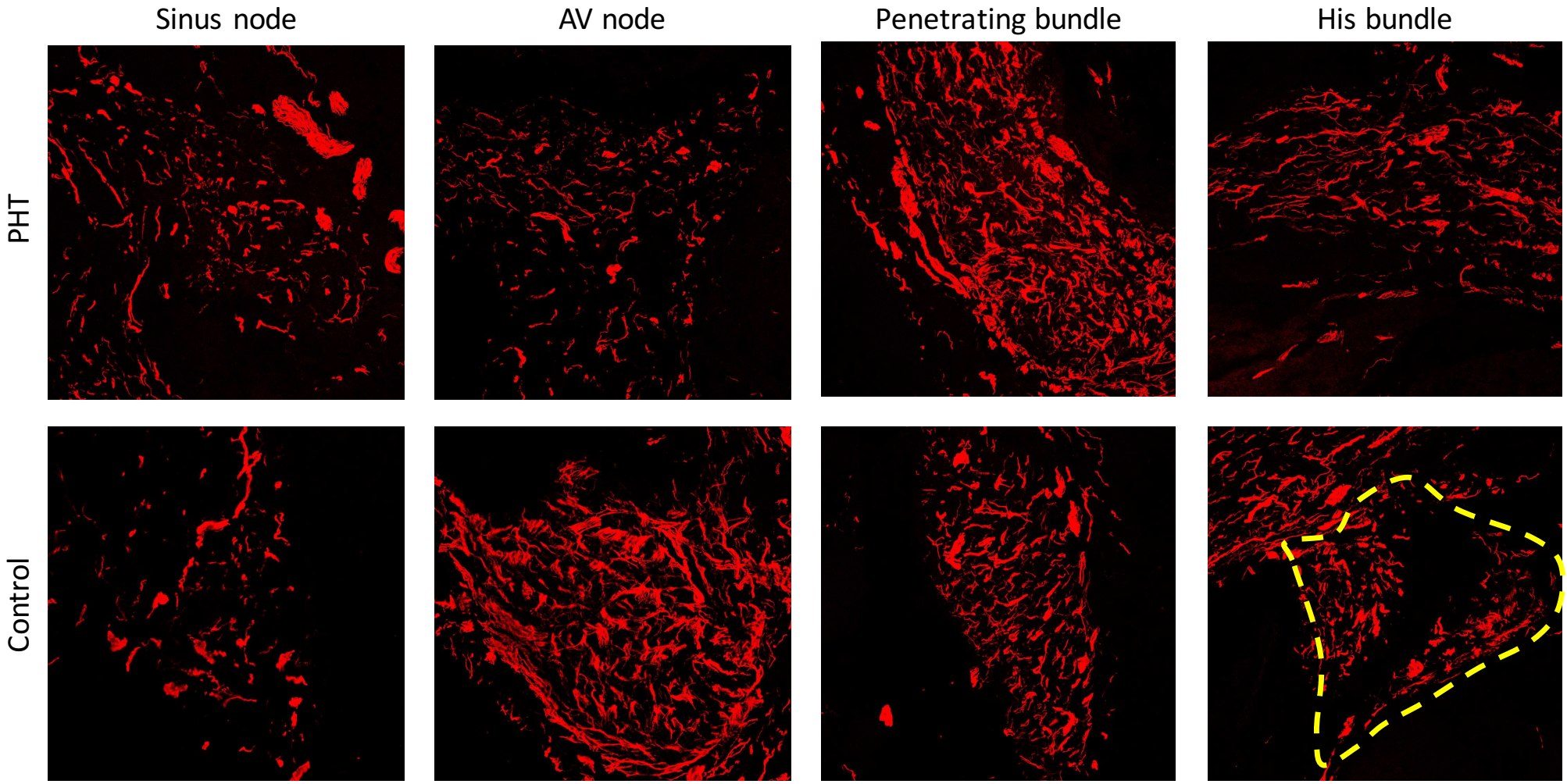

Fig. S7. Immunohistochemical labelling of neurofilament 150 (red signal; sympathetic neurone marker) in four parts of the cardiac conduction system including the AV node in control and PHT rats. The His bundle in the control rat is outlined in yellow.

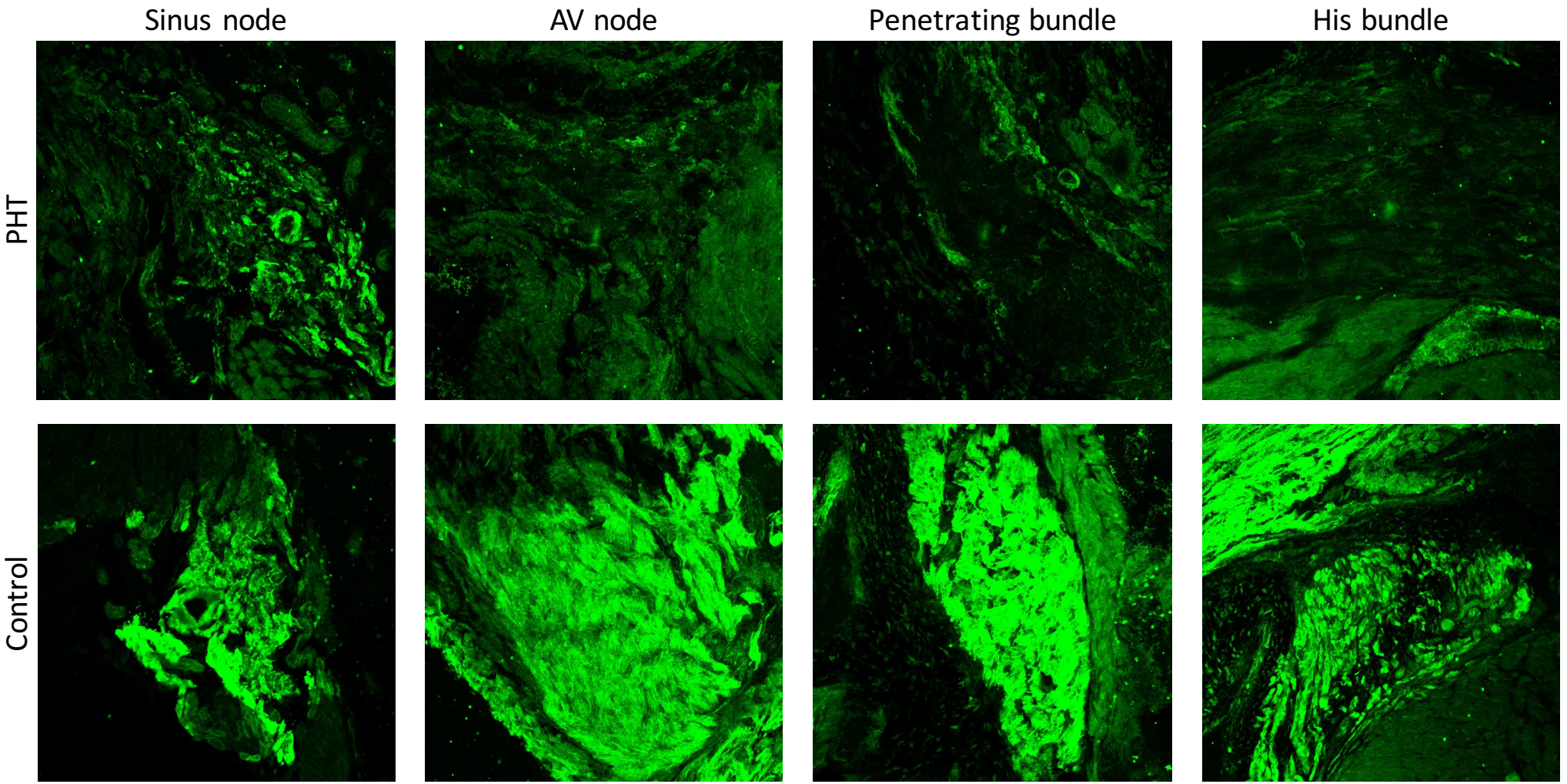

Fig. S8. Immunohistochemical labelling of HCN4 (green signal) in four parts of the cardiac conduction system including the AV node in control and PHT rats.